Acta Materialia 257 (2023) 119072

Contents lists available at ScienceDirect

Acta Materialia

journal homepage: www.elsevier.com/locate/actamat

Revisited precipitation process in dilute Mg-Ca-Zn alloys

Z.H. Li [a,b,1], D. Cheng [c,1], K. Wang [c], E.R. Hoglund [c], J.M. Howe [c], B.C. Zhou [c], T.T. Sasaki [a,d,*], T. Ohkubo [a], K. Hono [a,b]

[a] National Institute for Materials Science, 1-2-1 Sengen, Tsukuba 305-0047, Japan
[b] Graduate School of Pure and Applied Science, University of Tsukuba, Tsukuba 305-8577, Japan
[c] Department of Materials Science and Engineering, University of Virginia, Charlottesville, VA 22904, United States
[d] Center for Elements Strategy Initiative for Structural Materials (ESISM), Kyoto University, Yoshida Honmachi, Sakyo, Kyoto 606-8501, Japan

ARTICLE INFO

Keywords:
Magnesium alloys
Precipitation
HAADF-STEM
3DAP
First-principles calculation

ABSTRACT

To obtain thorough understandings of precipitation process in heat-treatable Mg-Ca-Zn alloy, we revisited the precipitation process of a Mg-0.3Ca-0.6 Zn (at.%) dilute alloy during isothermal aging at 200 °C using an aberration-corrected scanning transmission electron microscope, atom probe tomography, and first-principles calculations. The monolayer G.P. zones form on the $(0002)_\alpha$ plane in the peak-aged condition and transform into tri-atomic layer η'' and η' plates with a thickness of a single unit-cell height. The η' plates, then, form in pairs and stacks with energetically favorable 4–5 atomic layers of pure magnesium between the plates. While such a transformation path is similar to that seen in Mg-RE-Zn alloys (RE: rare-earth elements), the unique structure of coarse η_1 plates that precipitate after the η' plates leads to a different precipitate microstructure evolution from the Mg-RE-Zn system. The η_1 phase ($Mg_7Ca_2Zn_3$) is unevenly distributed in the matrix after 100 h of aging and finally evolves to the equilibrium η phase ($Mg_{10}Ca_3Zn_6$) phase with a hexagonal structure. First-principles calculations of energetics were performed to further identify the crystal structure and stability of the precipitates, supporting the following new precipitation sequence:

S.S.S.S. → G.P. zones → η'' → η' → η' pairs and stacks / η_1 → η

1. Introduction

Broad interests in lightweight magnesium (Mg) alloys have been provoked by the compelling weight-saving demand in the transportation and medical sectors [1,2]. Among recently developed Mg alloys, heat-treatable Mg-Ca-Zn alloys are potential candidates for various applications, including structural and biomedical applications [3–9]. The rapid age-hardenability of Mg-Ca-Zn dilute alloys led to good combinations of extrudability and strength in extrusions and formability and strength in sheets that had never been achieved in commercial Mg alloys [3–6]. The precipitation-hardened Mg-Ca-Zn alloys also exhibit good creep resistance and biocompatibility [6–9]. While the wrought alloys are heat-treated in under-aged or peak-aged conditions to use a high precipitation-strengthening effect [5], the creep-resistant alloys are over-aged at elevated temperatures [7], and the precipitate distribution significantly affects the degradation behavior in the biodegradable alloys [8,9]. Therefore, an in-depth understanding of the whole precipitation process in the Mg-Ca-Zn alloy is crucial to correlate the microstructure with properties, providing guidelines for further improvements of in-service performance.

The precipitation sequence in the Mg-Ca-Zn alloy was proposed in the literature as follows [10], and Table 1 summarizes the structures and compositions of the precipitates:

S.S.S.S. → α-Mg + ordered Guinier Preston (G.P.) zones → α-Mg + η' → α-Mg + η

In previous experimental studies [4,6,11-14], the G.P. zone was suggested to be a monolayer precipitate (hexagonal, $a = 0.56$ nm) forming on the $(0002)_\alpha$ plane of the Mg matrix with Ca and Zn atoms six-fold coordinated by Mg atoms. A recent density functional theory (DFT) study considered detailed configurations of Ca and Zn and suggested several structures consistent with experimentally reported diffraction patterns and STEM images [15]. In the suggested structures,

---

* Corresponding author.
E-mail address: SASAKI.Taisuke@nims.go.jp (T.T. Sasaki).

[1] These authors contributed equally to this work.

https://doi.org/10.1016/j.actamat.2023.119072
Received 4 January 2023; Received in revised form 11 May 2023; Accepted 5 June 2023

Ca atoms are six-fold coordinated by Mg or Zn atoms in the monolayer G.P. zones, and the most stable one is consistent with the measured Ca/Zn ratio (*i.e.*, ~ 1:1 [4,6]). However, the structure and composition of the metastable η' and equilibrium η phases are still under debate. The η' phase is a thin plate-like precipitate forming on the $(0002)_\alpha$ planes with a hexagonal structure ($P6_3/mmc$, a = 0.56 nm, c = 1.04 nm) in Mg-0.6Ca-0.4 Zn (at.%) alloy [16], while Oh-ishi et al., reported it has a similar monolayer structure to that of the G.P. zone in Mg-0.3Ca-0.6 Zn (at.%) alloy [13]. In addition, the η' single plates gradually form in plate pairs during over-aging [12]. Since such precipitate microstructure evolution is similar to that of γ'' phase in the Mg-RE-Zn (RE: Y or Gd) alloys, a more complicated precipitation sequence may be expected in the Mg-Ca-Zn dilute alloy like the following one, which is well established in the Mg-RE-Zn alloys [17–20];

$$\text{SSSS} \rightarrow \alpha\text{-Mg} + \text{ordered G.P. zones} \rightarrow \alpha\text{-Mg} + \gamma'' \rightarrow \alpha\text{-Mg} + \gamma' \rightarrow \alpha\text{-Mg} + \gamma + \delta$$

Different structures and compositions have been also reported for the equilibrium η phase depending on the alloy compositions. The η phase is a Mg_2Ca structure type phase with a hexagonal structure ($P6_3/mmc$, $a = 0.62$ nm, $c = 1.01$ nm) in Mg-0.6Ca-0.4 Zn (at.%) alloy, and has different orientation relationships (ORs) depending on the shape as listed in Table 1. However, a trigonal structure ($P\bar{3}1c$, $a = 0.97$ nm, $c = 1.01$ nm) with a chemical composition of $Ca_2Mg_6Zn_3$ was reported for the η phase in Mg-1Ca-2.3 Zn (at.%) alloy [21,22]. More recently, Schäublin et al. analyzed the precipitates formed in an as-extruded Mg-0.2Ca-0.6 Zn alloy and concluded that the structure of the ternary phase is hexagonal ($P6_3/mmc$, a = 0.96 nm, c = 1.00 nm) with a composition close to $Ca_2Mg_5Zn_5$ or $Ca_3Mg_{11}Zn_4$. [23–25].

Mg-0.3Ca-0.6 Zn (at.%) alloy exhibits the largest age-hardening response in the precipitation hardenable Mg-Ca-Zn system [13]. Therefore, the clarification of the precipitation sequence of this particular alloy composition would provide baseline knowledge for understanding the precipitate microstructures in the Mg-Ca-Zn dilute alloys. In this study, we thoroughly analyzed the precipitate microstructure evolution in the Mg-0.3Ca-0.6 Zn (at.%) alloy during artificial aging at 200 °C which is close to the aging temperature for wrought alloys and service temperature for creep-resistant ones, and unambiguously established the precipitation sequence in the Mg-Ca-Zn system. Furthermore, the atomic structures of metastable η'', η', and η_1 phases and equilibrium η phase are deduced, which are not only thermodynamically stable based on first-principles calculations, but also fulfill the structural and compositional information from STEM and 3DAP measurements. The phase stability of each precipitate type in first-principles calculations provides the thermodynamic rationale for the precipitation sequence.

2. Experimental and computational methods

Alloy ingots with a nominal composition of Mg-0.3Ca-0.6 Zn in at.% (Mg-0.5Ca-1.6 Zn in wt%, ZX20) were prepared from high-purity Mg (99.9%), Zn (99.99%) and Mg-30 wt.% Ca master alloy by induction melting in a steel crucible and casting into a steel mold in an argon (Ar) atmosphere. Hereafter, the alloy is denoted as ZX20. The chemical composition of the alloy was measured using inductively coupled plasma (ICP) analysis to be Mg-0.32Ca-0.61 Zn in at.%, and the impurity contents are significantly lower than the Ca and Zn contents. The ingots were encapsulated in He-filled Pyrex tubes for solution treatment at 520 °C for 2 h and then quenched into water. 2-mm-thick samples sectioned from the as-quenched ingots were subsequently aged in an oil bath at 200 °C for various times. The hardness value for each aging condition was measured by averaging 10 individual indentations using a Vickers hardness tester under a load of 0.3 kg.

(S)TEM observations were carried out using Thermo Fischer Scientific Titan G^2 80–200 TEMs equipped with a probe corrector and a Super-X energy-dispersive X-ray (EDX) spectrometer operating at 200 kV. Thin foil samples for STEM observations were prepared by punching 3 mm diameter discs and twin-jet electro-polishing using electrolyte of 5.3 g LiCl, 11.16 g $Mg(ClO_4)_2$, 500 ml methanol, and 100 ml 2-butoxy-ethanol at about −50 °C with a voltage of 90 V. After electropolishing, the foils were cleaned using ion-milling (Gatan PIPS) at 2 kV for 20 min. The thickness of TEM foils was measured using the convergent beam electron diffraction under a two-beam condition [26]. The atomic-resolution HAADF-STEM images were Fourier filtered using a Gatan Digital-Micrograph software. To minimize the effect of the surrounding matrix on the chemical quantification of coarse precipitates, EDS spectra were acquired near the edge areas of TEM thin foils, where the matrix is not expected to be included along the thickness direction. In addition, at least five measurements were performed for each precipitate with the analyzed region in the center of the precipitate to further reduce the errors caused by the matrix contribution. Simulation of high-angle annular dark-field (HAADF) images was carried out using the *xHREM* software developed by HREM Research Inc. based on the fast Fourier transform (FFT) multi-slice method [27]. The simulation parameters of acceleration voltage (200 kV), beam convergence semi-angle (17.9 mrad), HAADF detector radius (β_{inner} = 69 and β_{outer} = 200 mrad), defocus (0.4 nm), the third and fifth order spherical aberration (C3 = 0.5 mm and C5 = 0 mm), 2-fold astigmatism (A1 = 2.5 nm) were the same as experimental conditions. The dependence of image contrast on thickness is simulated up to 100 nm, and the optimized thickness values were selected to make a good match between experimental and simulated images. 3D atom probe (3DAP) analysis was performed using a local electrode atom probe (CAMECA LEAP 5000 XS) in voltage pulse mode at a temperature of 30 K. Sharp needle-like specimens for the

Table 1
Reported strengthening precipitates in dilute Mg-Ca-Zn alloys.

Phase	Ref.	Structure	composition	Lattice parameter, nm	Morphology	Orientation relationship
G.P. zone	[4,11-14,15]	hcp	$Mg_2(Ca,Zn)$ MgCaZn	$a = 0.56$ nm	monolayer $(0001)_\alpha$ disk	$[10\bar{1}0]_{G.P.}// [11\bar{2}0]_\alpha$
η’	[16]	hcp, $P6_3/mmc$	MgCaZn	$a = 0.56$ nm, $c = 1.04$ nm	$(0001)_\alpha$ plate	$(0001)_{\eta'} // (0001)_\alpha$, $[2\bar{1}\bar{1}0]_{\eta'} // [10\bar{1}0]_\alpha$
	[12]	hcp	—	$a = 0.56$ nm	$(0001)_\alpha$ plate	$[10\bar{1}0]_{\eta'} // [11\bar{2}0]_\alpha$
η	[16]	hcp, $P6_3/mmc$	$Mg_2(Ca,Zn)$	$a = 0.62$ nm, $c = 1.01$ nm	$(0001)_\alpha$ plate	$(0001)_\eta // (0001)_\alpha$, $[2\bar{1}\bar{1}0]_\eta // [10\bar{1}0]_\alpha$
	[12]	hcp, $P6_3/mmc$	$Mg_2Ca(Zn)$	$a = 0.58$ nm, $c = 0.94$ nm	rectangular shaped	$(0001)_\eta // (01\bar{1}0)_\alpha$, $[\bar{1}2\bar{1}0]_\eta // [2\bar{1}\bar{1}0]_\alpha$ and $(0001)_\eta // (0001)_\alpha$, $[\bar{1}2\bar{1}0]_\eta // [01\bar{1}0]_\alpha$
	[13,21,22]	trigonal, $P\bar{3}1c$	$Ca_2Mg_6Zn_3$	$a = 0.97$ nm, $c = 1.01$ nm	ellipsoidal shaped rhombus shaped cuboidal shape	$(10\bar{1}0)_\eta // (10\bar{1}0)_\alpha$, $[0001]_\eta // [0001]_\alpha$ $(0001)_\eta // (1\bar{2}10)_\alpha$, $[1\bar{2}10]_\eta // [\bar{1}010]_\alpha$ $(11\bar{2}0)_\eta // (0001)_\alpha$, $[0001]_\eta // [11\bar{2}0]_\alpha$, and $(11\bar{2}0)_\eta // (0001)_\alpha$, $[0001]_\eta // [21\bar{3}0]_\alpha$
	[23–25]	hcp, $P6_3/mmc$	$Ca_2Mg_5Zn_5$	$a = 0.96$ nm, $c = 1.00$ nm	-	-

3DAP analysis were prepared by the focused ion beam (FIB) lift-out and annular milling techniques using a FEI Helios G4 UX. The statistical and chemistry of precipitates in the selected volume were analyzed using a maximum separation algorithm in the IVAS™ 3.8.14 software. We determined the parameters of separation distances ($d_{\max} = 0.6 \sim 0.8$), minimum number of solutes ($N_{\min} = 8{\sim}10$), envelop distances ($L = 0.6 \sim 0.8$), and erosion distances ($d_{\mathrm{erosion}} = L$) based on the nearest neighbor approach described elsewhere [28,29], and optimized separately for each aging condition and precipitate type to avoid the unacceptable artifacts.

The atomic structures of precipitates were determined based on symmetry from diffraction pattern, composition from 3DAP analysis, contrast from STEM and thermodynamic stability from first-principles calculations. For a given structural template, numerous unique atomic structures exist depending on the atomic decoration of the lattice sites in the template. Based on the prototypical template from experiments, all the ordered structures are enumerated with the size of unit cell determined by diffraction pattern and STEM images. Here "enumerated" refers to the process of listing or generating all possible configurations with distinct occupations of Mg, Zn or Ca. The experimentally measured symmetry, compositions and SAED patterns were used to screen the atomic structures. For the disordered or partially disordered structures, the random distribution of solutes on the structural template is modeled using the special quasi-random structures (SQS) [30,31], where the correlation between solutes in a small cell mimics the completely random distribution of solutes in an infinitely large supercell. The Alloy Theoretic Automated Toolkit (ATAT) is used to enumerate ordered structures and build SQS [32]. When optimizing the correlations between solutes in SQS, the cut-off distances for pair, triplet and quadruplet clusters were at least 9.91, 6.39 and 5.54 Å.

After the candidate structures were chosen, first-principles electronic structure methods based on density functional theory (DFT) were performed to optimize the structures and calculate their formation energies [33,34]. The ion-electron interaction was described by the projector augmented plane-wave method [35] and the exchange-correlation functional was described by an improved general gradient approximation of Perdew-Burke-Ernzerhof [36], as implemented in the Vienna ab initio simulation package (VASP, version 5.4) [37,38]. The detailed DFT settings and the methods for stability analysis can be found in our previous work [15]. In addition to agreeing with the symmetry and composition from experiments, a candidate structure is chosen only if it does not collapse during structural optimization (*i.e.*, mechanical stability) and has negative formation energy (*i.e.*, thermodynamic stability) with respect to pure metals. Note that formation energies per solute are used to compare the relative stabilities of precipitates in different compositions and reflect the changing chemical potential of the observed precipitates during the aging process [39,40]. In DFT calculations, the atomic positions were allowed to relax while the cell shape and volume were fixed for the early-stage precipitates (*i.e.*, η' and η'') to mimic the constraint from the Mg matrix. Meanwhile, all degrees of freedom were relaxed for the precipitates with bulk structures (*i.e.*, η_1 and η).

3. Experimental results

Fig. 1 shows the variation in Vickers hardness for the ZX20 alloy during isothermal aging at 200 °C. The ZX20 alloy has a hardness value of 50.1 ± 1.1 HV in the as-quenched condition, and exhibits a substantial increase to the peak hardness of 63.6 ± 1.3 HV in only 0.3 h. After a short plateau until ~ 3 h, the hardness gradually decreases to 40.3 ± 1.2 HV after 1000 h.

Figs. 2a through f show the HAADF-STEM images and SAED patterns obtained from the samples aged at 200 °C for various time. The corresponding bright-field (BF) TEM images are shown in Figure S.1. Note that the HAADF-STEM and BF-TEM images were acquired from a $[1\bar{1}00]_\alpha$ zone axis, and the SAED patterns were taken from both $[0001]\alpha$ and $[1\bar{1}00]\alpha$ zone axes. Although precipitates are not clearly visible due to the low magnification of the HAADF-STEM image at 0.1 h, Fig. 2a, the formation of extremely fine plate-like precipitate is expected on the $(0002)_\alpha$ planes because faint diffraction spots and streaks are visible at the $1/3(11\bar{2}0)_\alpha$ and $2/3(11\bar{2}0)_\alpha$ in the SAED patterns [6]. At the peak hardness of 0.3 h, brightly imaged fine plate-like precipitates with an average diameter of 3.6 ± 0.8 nm are densely distributed on the $(0002)_\alpha$ planes, Fig. 2b. These fine plates are identified as the G.P. zones according to the extra reflections and continuous streaks in the SAED patterns [11]. The strain contrast surrounding the G.P. zone indicates the coherent interface with the Mg matrix, Fig. S.1a. The fine plates are coarsened by over-aging for 2 h and 10 h as their average diameter increases to ~ 7.8 ± 1.3 and ~ 14.7 ± 3.2 nm, respectively, Figs. 2c and d. The SAED patterns of 2 and 10 h-aged samples show similar features to those observed in 0.3 h-aged sample, indicating that ordered structures remain within these large plates. The strain contrast is also clearly observed at the long sides of plates, Fig. S.1b and c. The plate-like precipitate forms in pairs followed by stacks by prolonged aging, as shown in the HAADF-STEM images obtained from the 100 h- and 300 h-aged samples, Figs. 2c and d. The average diameter of the plate pairs at 100 h aging is ~ 25.7 ± 5.6 nm and coarsened to ~ 45.3 ± 8.7 nm after 300 h aging. The extra reflections and strain contrast are still visible in the SAED patterns and the BF images, respectively, suggesting the retention of ordered structures and interfacial coherence in these plate pairs and stacks, Fig. S.1d and e.

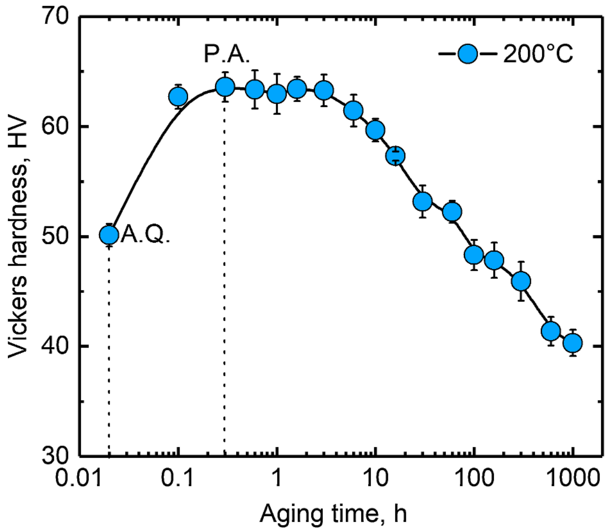

Fig. 1. Variations in Vickers hardness as functions of aging time for the ZX20 alloy during artificial aging at 200 °C. Note that A.Q. and P.A. stand for as-quenched and peak-aged condition, respectively.

Figs. 3a through c show atomic-resolution HAADF-STEM images of the nanoscale precipitates in the 0.3 h, 2 h, and 10 h aged samples, respectively. The ordered G.P. zone in the 0.3 h-aged sample is a monolayer plate, Fig. 3a. The $[11\bar{2}0]\alpha$ image shows bright columns containing either Ca or Zn arranged closely on a single $(0002)_\alpha$ plane, while a periodical arrangement of Zn/Ca-rich columns with an interval of every two columns are observed along the $[1\bar{1}00]\alpha$. The intensity profile across the G.P. zone and the $(0002)_\alpha$ planes shows that the interplanar spacing between two adjacent $(0002)_\alpha$ planes centering the G.P. zone is measured to be ~ 0.49 nm, which leads to a misfit of −0.058 along the direction normal to the $(0002)_\alpha$ habit plane assuming $d_{(0001)_\alpha}$ is 0.52 nm. Because the interspacing between the bright Zn/Ca-rich columns in the G.P. zone is measured to be ~ 0.48 nm in the $[1\bar{1}00]\alpha$ projection plane, the G.P. zone is proposed to have an ordered structure

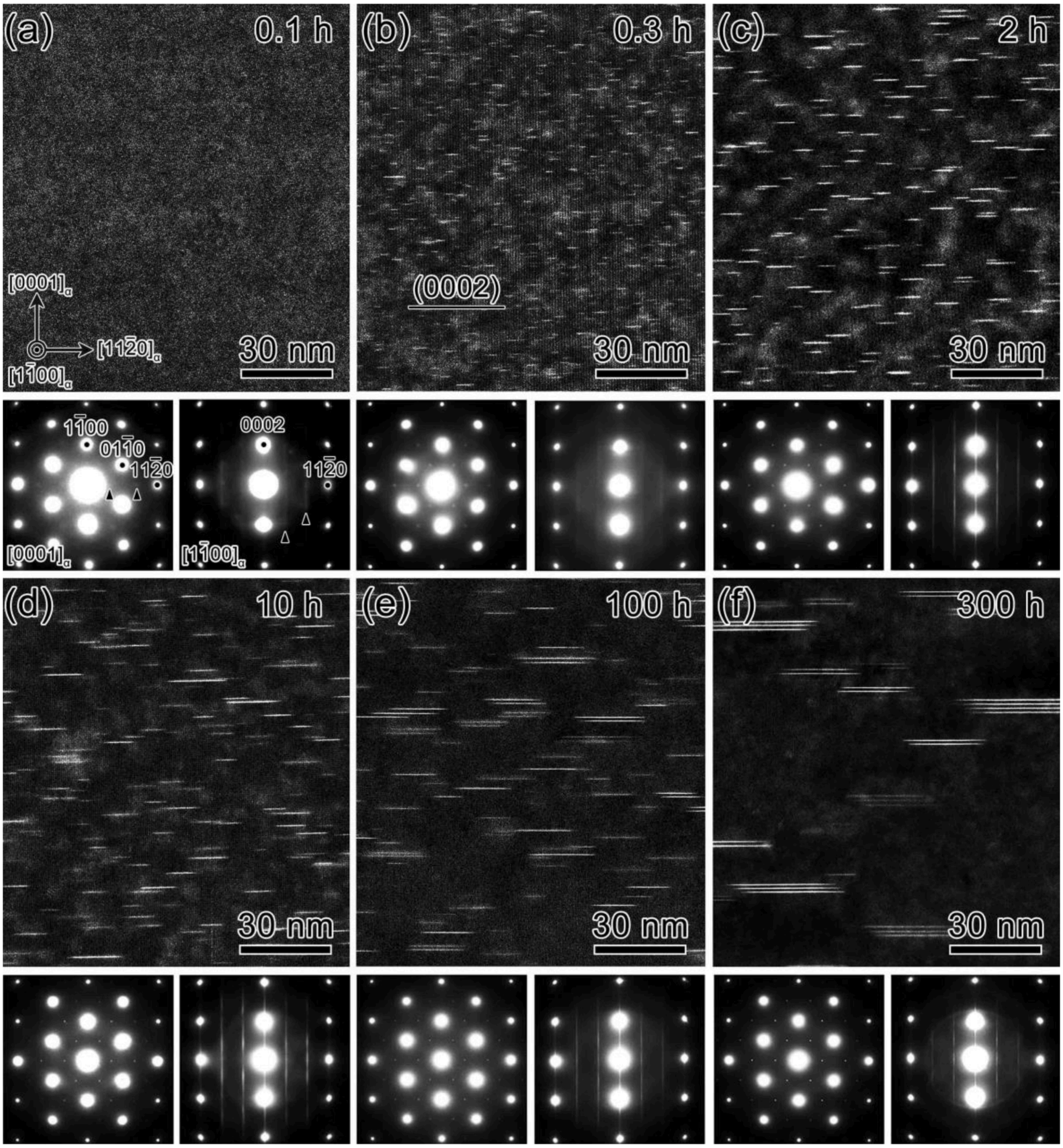

Fig 2. HAADF-STEM images and SAED patterns of the ZX20 alloy aged for (a) 0.1 h, (b) 0.3 h; peak-aged, (c) 2 h, (d) 10 h, (e) 100 h and (f) 300 h, respectively, at 200 °C. Note that the images were taken from the $[1\bar{1}00]\alpha$ zone axis, and SAED patterns were recorded from both $[0001]_\alpha$ and $[1\bar{1}00]\alpha$ directions.

with $a = 0.56$ nm, which in agreement with the one in the DFT calculations [15], as well as the experimental observations in Mg-Ca-Zn(-Zr) and Mg-RE-Zn-Zr alloys [11,13].

The monolayer G.P. zones transform into tri-atomic-layer plates designated as the η'' phase by aging for 2 h, Fig. 3b. The middle layer of the η'' shows the brightest contrast from the $[11\bar{2}0]\alpha$, indicating a strong Zn enrichment compared to the two side layers. The $[1\bar{1}00]\alpha$ image shows a similar atomic arrangement for all three layers with a periodicity of every two brighter columns separated by one dark column. The thickness of the η'' plate from the intensity profile is measured to be ~ 0.47 nm, leading to a slightly large lattice misfit of −0.096 compared to that of the G.P. zone. The HAADF-STEM images and SAED patterns suggest that the η'' phase has an ordered hexagonal structure ($P\bar{6}2$ m, $a = 0.56$ nm and $c = 0.47$ nm), which is similar to the γ'' phase in the Mg-Gd-Zn(-Zr) alloys [17,20].

The plate-like precipitates in the 10 h-aged sample are also tri-atomic-layer on the $(0002)_\alpha$ planes, Fig. 3c. Unlike the η'' phase, the atomic positions in the brightly imaged middle layer shift by a distance of $\sqrt{3}/6$ along each $[1\bar{1}00]_\alpha$ direction, which allowed us to identify it as the η' phase. The thickness of the η' is measured to be ~0.46 nm with a lattice misfit of −0.115, which is slightly larger than that of the η'' phase, −0.096. The η' phases are determined to be a hexagonal structure ($P\bar{6}2$ m, $a = 0.56$ nm and $c = 0.43$ nm) that is analogous to the γ'' phase observed in other Mg-Gd-Zn and Mg-Y-Zn-Ag-Zr alloys [18,41-43]. Considering the structural similarity, the OR between η'/η'' and the α-Mg matrix is described as $(0001)_{\eta'/\eta''}// (0001)_\alpha$, $[10\bar{1}0]_{\eta'/\eta''}// [11\bar{2}0]_\alpha$.

Fig. 4a shows a 3D atom map of Mg, Ca, and Zn obtained from the 0.3 h-aged sample. The Ca and Zn are enriched within densely dispersed plates with a number density of ~ $1.2 \times 10^{24}\ m^{-3}$. The plate diameter dependence of the Zn/Ca ratio are measured by the maximum separation algorithm from a larger volume of 200 × 40 × 40 nm^3. The Zn/Ca ratio exhibits wide scatter within a small diameter of less than 1 nm due

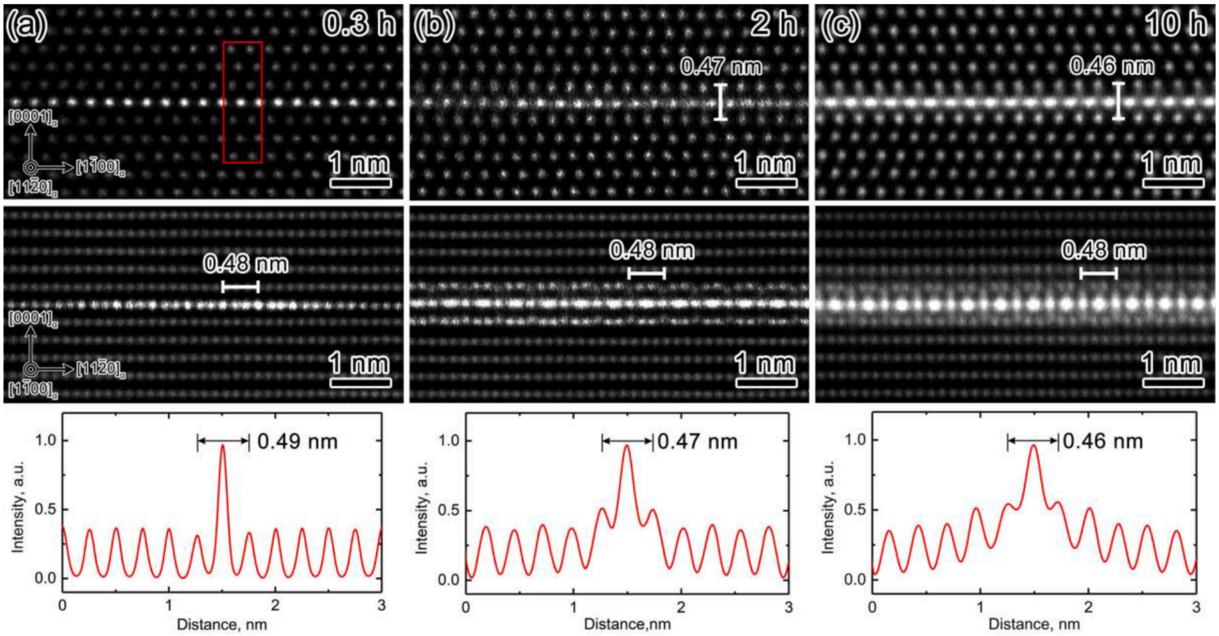

Fig. 3. Atomic-resolution HAADF-STEM images and intensity profiles measured across the nanoscale precipitates observed in (a) 0.3 h, (b) 2 h, (d) 10 h at 200 °C. Note that the images on the upper and middle row are taken from the zone axes of $[11\bar{2}0]\alpha$ and $[1\bar{1}00]\alpha$, respectively. (For interpretation of the references to colour in this figure legend, the reader is referred to the web version of this article.)

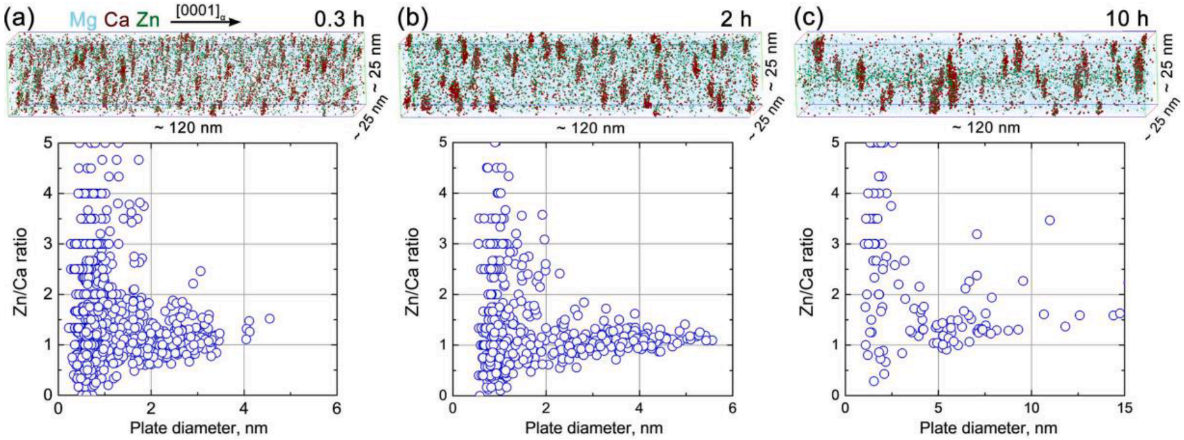

Fig. 4. 3D atom maps of Mg, Ca, and Zn, and plots of variations of Zn/Ca ratio as functions of the plate diameter in the ZX20 alloys aged for (a) 0.3 h, (b) 2 h and (c) 10 h, respectively.

to the random solute fluctuations in the matrix [44–46], and narrower distributions with increasing plate size. Most plates in the diameter of 1 ~ 3 nm have the Zn/Ca ratio varied from 0.6 to 1.4 with an average of ~ 1, which is close that of the G.P. zones [4,15]. The Ca/Zn-rich regions become more evident with the decreased number density in the 2 h (~ 4.5 × 10^{23} m^{-3}) and 10 h-aged (~ 1.6 × 10^{23} m^{-3}) samples, respectively, Figs. 4b and c. Meanwhile, the average Zn/Ca ratio of plates also gradually increases with the aging time. The 2 h-aged sample shows varied Zn/Ca ratio of 0.8–1.3 (average ~1.1) in the plate diameter of 2 ~ 6 nm, Fig. 4b, which is slightly higher than that of the G.P. zones. The variation of Zn/Ca ratio in the 10 h-aged sample further increases to ~ 1–2 (average ~ 1.5) in a larger plate diameter of 4–15 nm, Fig. 4c, indicating the transformation from the G.P. zone to the η'/η'' phase. Note that the scattered points in the diameter range of 5 ~ 10 nm are from plates located near a zone line with a high concentration of Zn, which leads to the overestimation of Zn/Ca ratios due to the preferential loss of Mg and Ca atoms by trajectory aberrations [47].

Fig. 5 shows an atomic-resolution HAADF-STEM image of the precipitates obtained from the 100 h- and 300 h-aged samples. A η' plate pair composed of two single η' plates are observed from the $[11\bar{2}0]\alpha$ and $[10\bar{1}0]\alpha$ zone axes with an interplanar spacing of ~ five α-Mg layers, Figs. 5a and b. Further aging to 300 h leads to the precipitation of the other two η' plates to form the η' plate stack, and the number of the α-Mg layer between the neighboring η' plates is five in most cases, Figs. 5c and d. In the 300 h-aged sample, some η' plate stacks may also transform into a coarse plate-like precipitate designated as η_1 phase, where the η' plates and an atomic layer enriched with Zn (and Ca) are alternatively stacked as seen from $[11\bar{2}0]\alpha$ and $[10\bar{1}0]\alpha$ images, Figs. 5e and f. The corresponding FFT pattern along the $[10\bar{1}0]\alpha$, Fig. 5g, shows that the $(0002)_\alpha$ and $(11\bar{2}0)_\alpha$ reflections are divided by three and two extra spots, respectively, indicating that the $d_{(0001)\eta1}$ and $d_{(1\bar{1}00)\eta1}$ are about four and three times that of $d_{(0002)_\alpha}$ and $d_{(11\bar{2}0)_\alpha}$. The unit cell height of the η_1 phase is measured to be ~ 0.96 nm, leading to a lattice misfit of −0.077 smaller than that of the η' phase. To obtain the chemical composition of the η_1, the STEM-EDS mapping was performed in an area

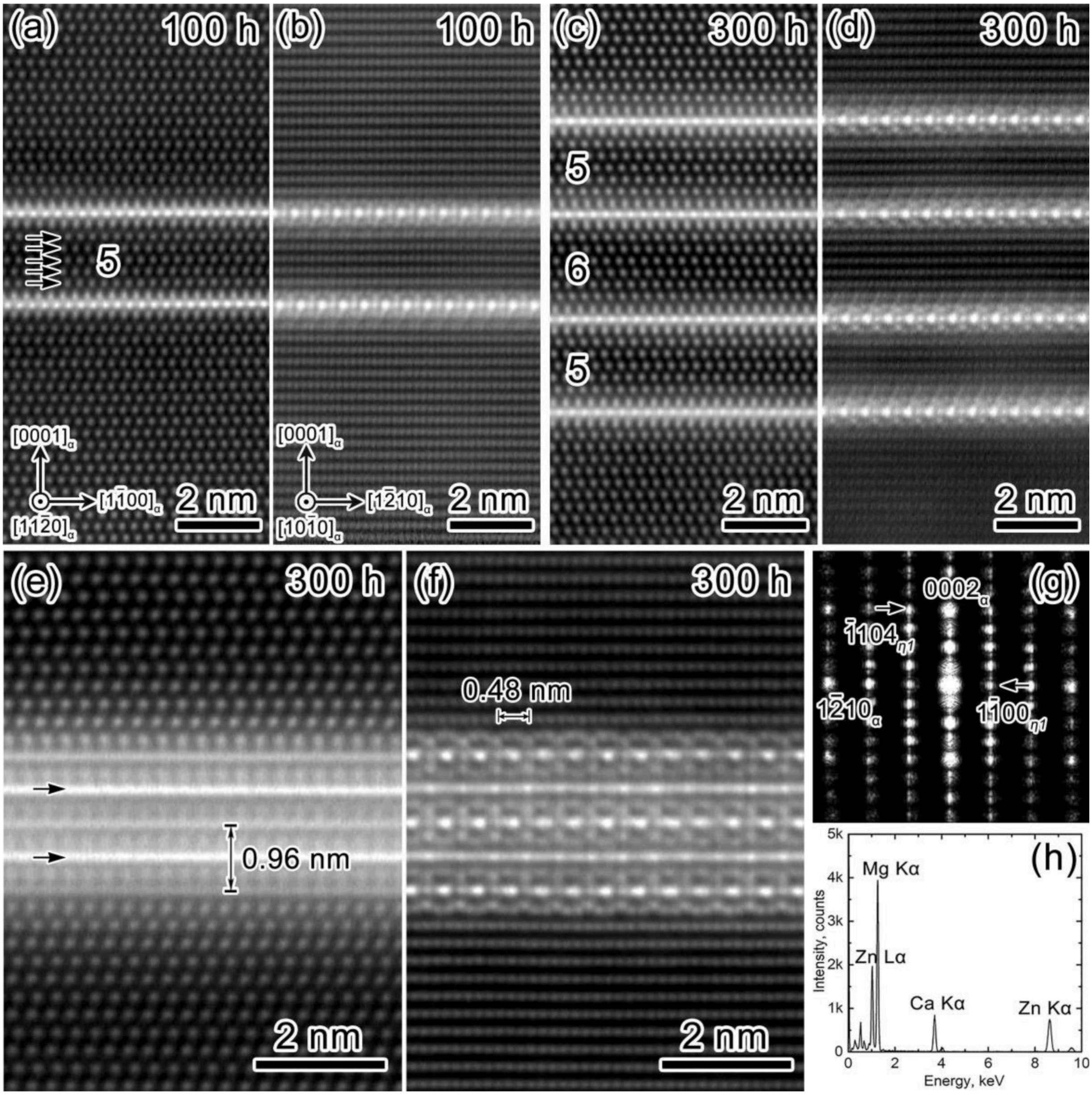

Fig. 5. Atomic-resolution HAADF-STEM images of the (a,b) η' plate pair seen in 100 h-aged sample and (c,d) η' plate stack seen in 300 h-aged sample, respectively. (e,f) is a part of η_1 phase precipitate observed in 300 h-aged sample. (g) and (h) are the FFT pattern and EDX spectrum obtained from the η_1 phase, respectively. Note that (a,c,e) and (b,d,f) are taken from the zone axes of $[11\bar{2}0]\alpha$ and $[10\bar{1}0]\alpha$, respectively.

of 13 × 9 nm^2 including the η_1 plate and surrounding matrix. The standardless quantitative analysis from the EDX spectrum in the center area of the plate (Fig. 5h) indicates that the η_1 phase has an average composition of Mg-14.2 ± 2.1Ca-21.6 ± 1.2 Zn (at.%). The above results suggest that the η_1 phase has a hexagonal structure (a = 0.56 nm, c = 0.96 nm) with a Ca/Zn ratio remaining ~ 1.5. The OR between η_1 and the α-Mg matrix is such that $(0001)_{\eta_1}// (0001)_\alpha$, $[11\bar{2}0]_{\eta_1}// [10\bar{1}0]_\alpha$.

Figs. 6a and b show low-magnification HAADF-STEM images of the ZX20 alloy aged for 1000 h taken from the $[11\bar{2}0]\alpha$ and $[0001]_\alpha$ zone axes, respectively. Among several precipitates with different shapes, typically observed precipitates are the rhombic-shaped plates lying on the $(0001)_\alpha$ planes as indicated by arrow 1. These basal precipitates are designated as η phase with an average length, width, and thickness of ~ 350±100, ~ 80±40, and ~ 30±10 nm, respectively. Some non-basal η precipitates also exist in the matrix, and the ones lying on the $\{10\bar{1}3\}\alpha$ planes (indicated by arrow 2) have a lath shape with an average length, width, and thickness of ~ 300±80, ~ 50±20 and 20±10 nm, respectively. The EDX spectrum as shown in Fig. 6c suggests a chemical composition of Mg-30.2 ± 1.1 Zn-16.4 ± 1.3 Ca (at.%) for the η phase. Fig. 6d shows the 3D atom map of Mg, Ca, and Zn obtained from the 1000 h-aged sample with the analysis direction parallel to the $[0001]_\alpha$ zone axis. The detected precipitate shows the long facets inclined ~ 32° to the $(0001)_\alpha$ plane, corresponding to the non-basal η as indicated in Fig. 6a. The interplanar spacing parallel to the $(0001)_\alpha$ plane is ~ 0.53 nm as clearly resolved in the magnified image across the precipitate. By the proximity histogram analysis based on the ~ 9% Ca isosurface, Fig. 6e, the composition of the η phase is determined to be Mg-29.4 ± 0.5 Zn-17.1 ± 0.4 Ca (at.%), which is in good agreement with the quantification results of the EDS analysis.

Nanobeam electron diffraction (NBED) patterns were taken from different crystallographic directions to determine the crystal structure of the η phase, Figs. 7a through c. At least five η precipitates for each orientation were measured to ensure the representativeness of the NBED patterns. Assuming the lattice parameters of the α-Mg matrix are a =

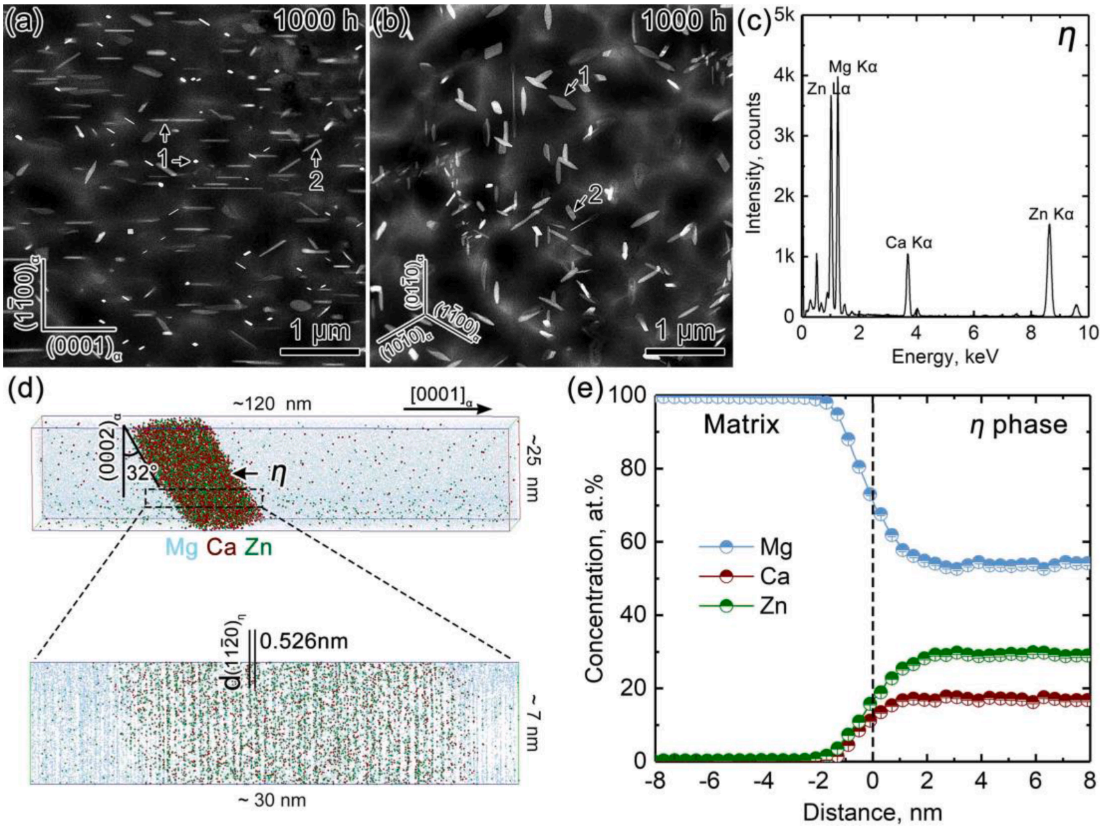

Fig. 6. Low-magnification HAADF-STEM images of the ZX20 alloy aged at 200 °C for 1000 h with the electron beam parallel to the (a) $[11\bar{2}0]\alpha$ and (b) $[0001]_\alpha$, respectively. (c) The EDX spectrum recorded from the η phase. (d) A 3D atom map of Mg, Ca, and Zn obtained from the 1000 h-aged sample with an enlarged 2D projection across the η phase. (e) Proximity histogram across the matrix/precipitate interface.

0.32 nm and $c = 0.52$ nm, these NBED patterns could be indexed based on a hexagonal structure with $a = 1.00$ nm and $c = 1.01$ nm. The point group and space group are provided as 6/mmm and $P6_3/mmc$, respectively, considering the symmetries and reflection conditions. (See Figure S.2 and S.3, Table S.1 and S.2 for the detailed information) [48–50]. Therefore, the structure of the η phase ($P6_3/mmc$, $a = 1.00$ nm, $c = 1.01$ nm) is similar to that of the $Ca_2Mg_5Zn_5$ ($P6_3/mmc$, $a = 0.96$ nm, $c = 1.00$ nm), while the measured Mg/Zn ratio is lower than the reported one [25]. From the atomic resolution HAADF-STEM images of the η phase taken from the $[0001]_\eta$, $[11\bar{2}0]_\eta$, and $[1\bar{1}00]_\eta$ zone axes, respectively. The atomic columns with the brightest and weakest imaging contrast are supposed to be enriched with Zn and Mg, respectively, while the ones with dim contrast are considered as co-occupation by Zn/Mg, Mg/Zn, or Ca atoms. To distinguish the difference in the imaging contrast among the columns, we performed the intensity profile analysis and revealed the locations of different types of atoms along the selected columns. Based on simple assumptions about mixed atomic ratios, the HAADF-STEM simulations were performed repeatedly until the imaging contrast in the simulated images is consistent with the experimental ones, as inserted in the atomic resolution HAADF-STEM images. As a result, the Zn/Mg and Mg/Zn ratio in the mixed atomic sites are determined to be 3:1 and 1:1 with an error margin of 1/4, respectively. The thermodynamic and mechanical stabilities of site occupancies are further verified by DFT calculations. The sample thickness used for the STEM simulations is ~ 35 nm. Therefore, the atomic model of η phase is supposed to have 38 atoms in the unit cell (6 Ca atoms, 2 Zn atoms, 14 Mg atoms, 12 Zn/Mg atoms, 4 Mg/Zn atoms) and a composition of $Mg_{10}Ca_3Zn_6$.

Figs. 8a and d show high-magnification HAADF-STEM images of basal and non-basal η precipitates in the 1000 h-aged sample viewed along the $[11\bar{2}0]_\alpha$ zone axis. The rhombic-shaped η basal plate (indicated by arrow 1 in Fig. 6) exhibits a spindle-shaped cross-section with ~ 50 nm in width and ~ 30 nm in thickness, while two pairs of facets with the long sides, *i.e.*, habit plane parallel to the $(\bar{1}103)_\alpha$ are observed for the lath-shaped η non-basal plate (indicated by arrow 2). Close inspection of the interfacial structures indicates that both η plates show fully coherent interfaces with the α-Mg matrix as one $(22\bar{4}0)_\eta$ plane matches well with one $(1\bar{1}01)_\alpha$ plane, Figs. 8b and e. The corresponding FFT images show the same OR of $(11\bar{2}0)_\eta$ // $(0001)_\alpha$, $[0001]_\eta$ // $[11\bar{2}0]_\alpha$ for both basal and non-basal η plates, Figs. 8c and 8f, while the long-side interface of the non-basal plate is rotated counter-clockwise for ~ 32° with respect to $(0001)_\alpha$.

4. Computational results and discussions

In this work, we performed an in-depth microstructure analysis to clarify the precipitation process of the ZX20 alloy during isothermal aging at 200 °C. According to the phase diagram reported by Schäublin et al. [25], the aging temperature of 200 °C for the presently studied ZX20 alloy is within the temperature range of 130 ~ 360 °C, where the precipitation of η phase is expected to be dominant. In contrast, two MgCaZn ternary phases of IM1 and IM3 coexist during aging below 130 °C, and the formation of the Mg_2Ca phase occurs instead of the IM3 phase during aging at 360 ~ 400 °C. Therefore, the crystal structures and precipitation sequence reported in the present work would be the base for understanding the precipitation behavior in Mg-Ca-Zn dilute alloys that may change depending on the aging temperature.

In this section, we propose the atomic structures for the observed metastable *η'', η', η₁* phases and equilibrium η phase based on the structural and compositional information in HAADF-STEM and 3DAP. The proposed structures were validated by their stabilities in DFT calculations, and the simulated STEM and SAED patterns. In the

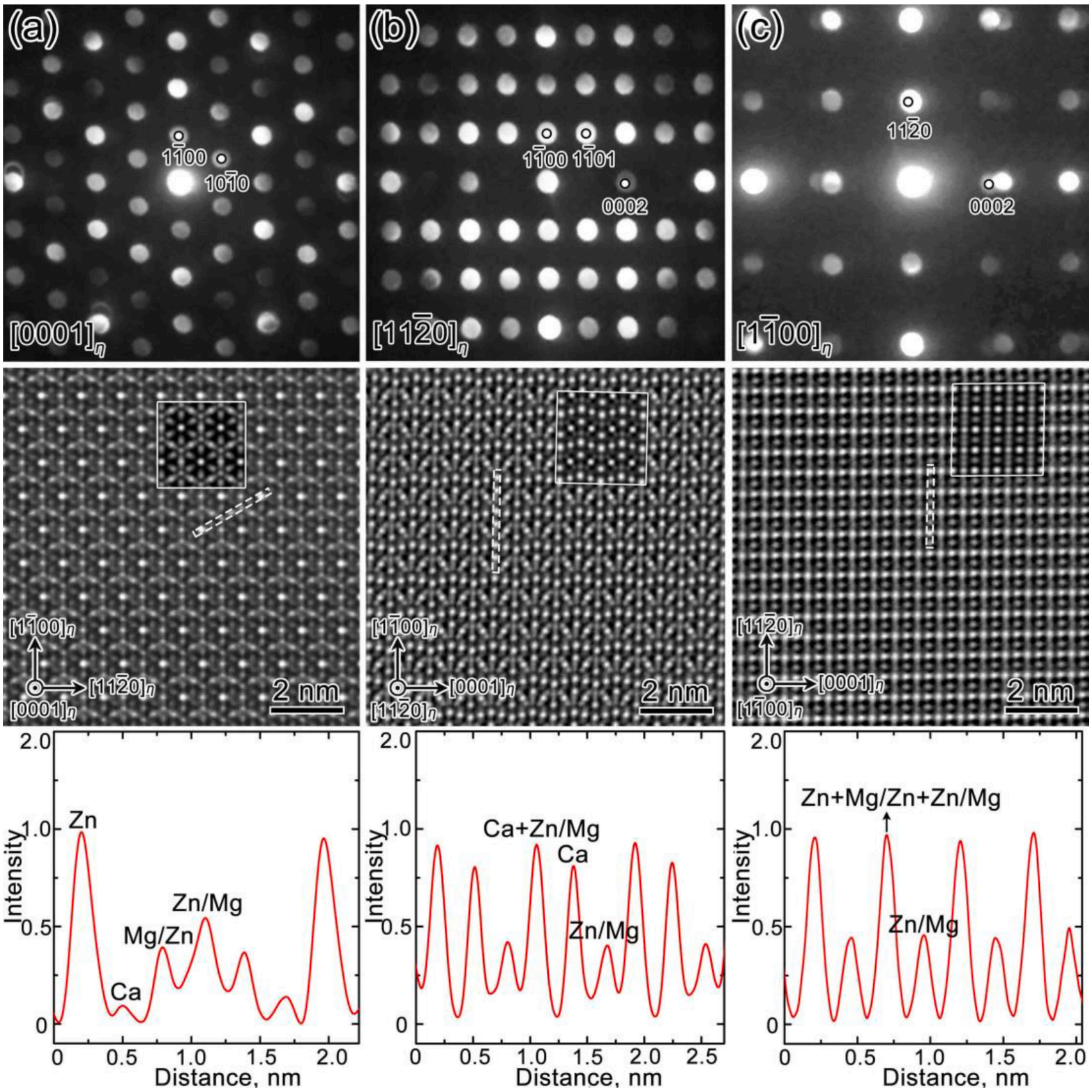

Fig. 7. The NBED patterns, atomic resolution HAADF-STEM images, and intensity profiles along selected atomic columns of the η phase taken from (a) $[0001]_\eta$, (b) $[11\bar{2}0]_\eta$, and (c) $[1\bar{1}00]\eta$ zone axes, respectively. Inserted are simulated images enclosed by white frames.

calculations, we found that there are usually several structures for each phase with the same structural template and similar formation energies but slightly different site occupations on the template (hence fluctuations in overall composition). The ones that best match the experimental information are chosen as the final candidates in the current work, and corresponding crystallographic information files (CIF) of proposed atomic structures are provided in the Supplementary Materials. The relative stabilities of the proposed structures of the precipitates in DFT provide the thermodynamic reasoning behind the observed precipitation sequence in the current experiments:

$$\text{S.S.S.S.} \rightarrow \text{G.P. zones} \rightarrow \eta'' \rightarrow \eta' \rightarrow \eta' \text{ pairs and stacks } / \ \eta_1 \rightarrow \eta$$

Distinguished from the monolayer G.P. zones, the η'' and η' phases are tri-atomic layer plates, as shown in Fig. 3. Both η'' and η' phases have similar hexagonal structures; $a = 0.56$ nm, $c = 0.47$ nm and $a = 0.56$ nm, $c = 0.46$ nm, respectively, but different Zn/Ca ratios within the plates; ~ 1.2 and 1.5, Figs. 4b and c. Because the η'' and η' are similar to those in HAADF-STEM images of γ'' precipitates in Mg-RE-Zn alloys, *i.e.*, tri-layer structures consisting of two undulating side layers and a middle layer [11,18,41-43], the atomic structures of the η'' and η' phases are constructed based on the reported structural template for γ'' precipitate.

Fig. 9 shows atomic models, simulated STEM images, and diffraction patterns of η'' phase embedded in the Mg matrix along the $[1\bar{1}00]_\alpha$ and $[11\bar{2}0]_\alpha$ directions. This phase is proposed to be $Mg_5Ca_2Zn_2$ with the Zn/Ca ratio of 1:1. Note that this Zn/Ca ratio approximates the statistical average of the composition fluctuation observed in 3DAP, Fig. 3b. In this tri-layer phase, the two side layers have an ordered pattern with Ca atoms six-folded coordinated by Mg atoms on the basal plane, where some Ca are randomly replaced by Mg with the Ca/Mg ratio of ~ 3:1 and some Mg atoms are replaced by Zn with the Mg/Zn of ~3:1, Fig. 9a. The Ca/Mg and Mg/Zn ratios are proposed according to the atomic column intensities in the two side layers in the experimental STEM image, Fig. 3b. The Mg-rich columns in the side layers of η'' are slightly brighter than the Mg columns in the matrix, which indicates some solutes are in these Mg-rich columns in the side layers. In our previous analysis of G.P. zones [15], we found that Zn atoms are favored compared with Ca atoms on the Mg-rich columns along $[1\bar{1}00]_\alpha$. Considering the similarity between the G.P. zones and the side layers in η'', some Mg atoms in the Mg-rich columns of the side layer of η'' are replaced with Zn. Furthermore, Ca-rich columns in the side layers are dimmer than or equally bright to the Mg-rich columns, indicating atoms with a smaller atomic number are on these sites. The ordered pattern on the two side layers of η'' corresponds to the streaks of the 1/3 and 2/3 $[11\bar{2}0]_\alpha$ on the

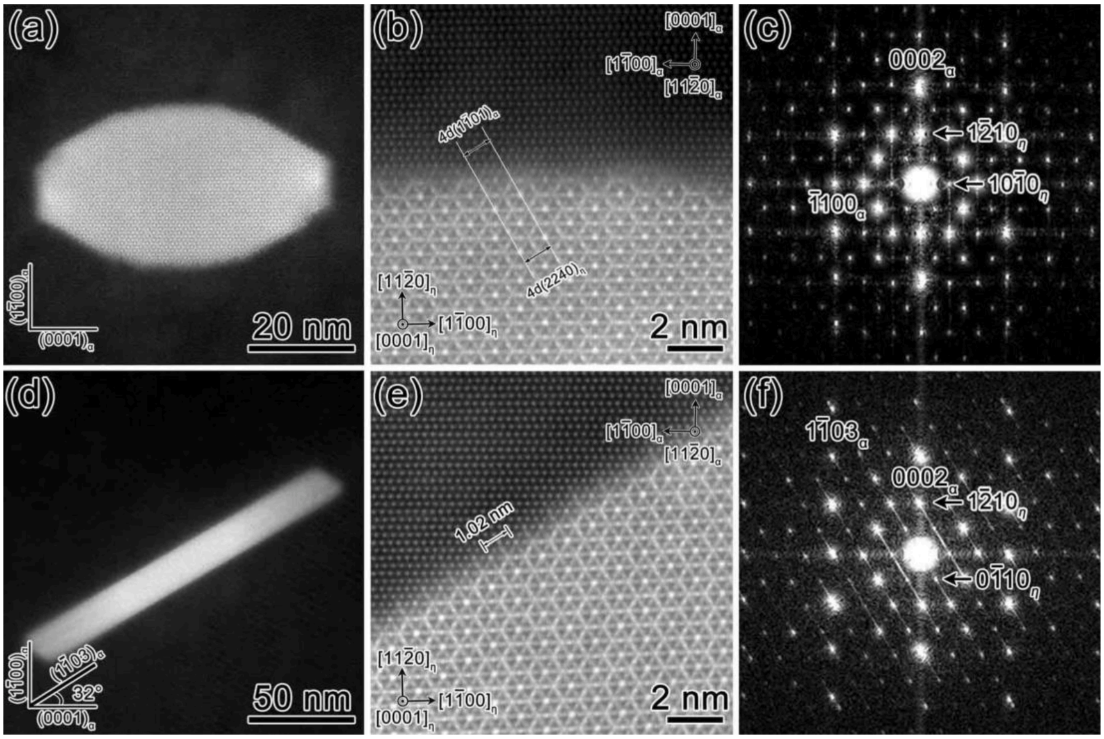

Fig. 8. (a,d) High-magnification HAADF-STEM images obtained from the basal and non-basal η precipitates indicated by arrow 1 and 2 in Fig. 7. (b,e) Atomic resolution HAADF-STEM images of interfacial structures, and (c,f) corresponding FFT patterns respectively. Note that electron beam is parallel to the $[11\bar{2}0]\alpha$.

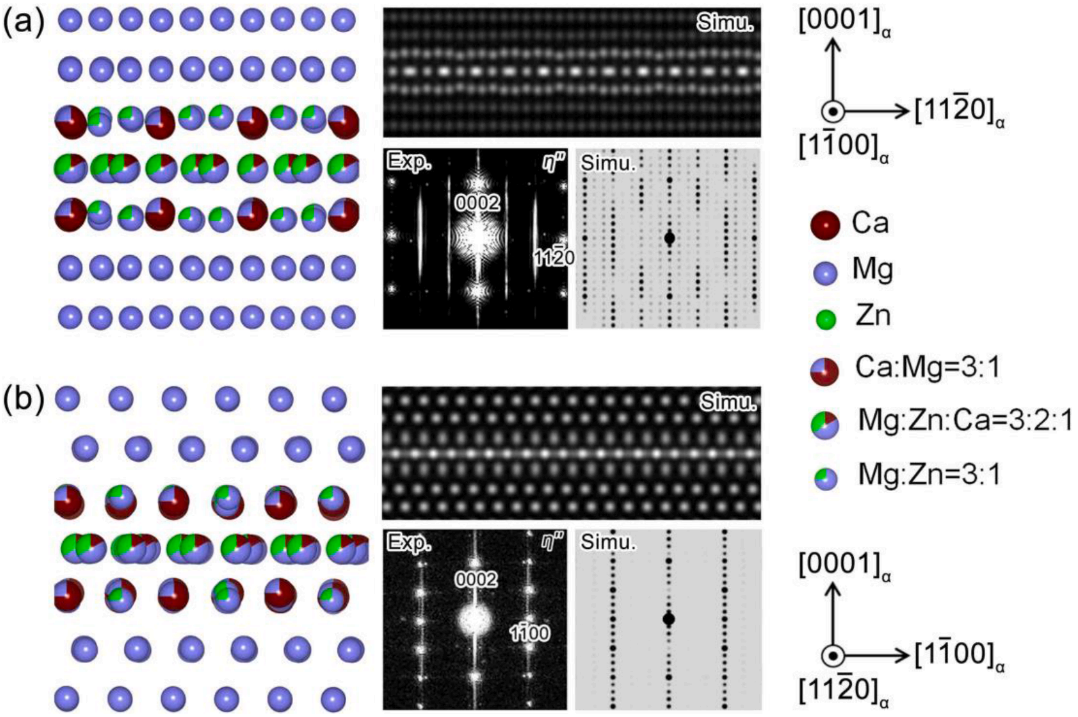

Fig. 9. The proposed atomic models, simulated STEM images, and diffraction patterns of the η'' phase embedded in Mg matrix viewed along the (a) $[1\bar{1}00]_\alpha$ and (b) $[11\bar{2}0]_\alpha$ directions.

experimental $[1\bar{1}00]_\alpha$ diffraction pattern, Fig. 9a. The middle layer contains Mg, Ca and Zn atoms distributed randomly with a ratio of 3:2:1 (mixed atomic symbols) with two columns closer to each other within each periodicity viewed along the $[1\bar{1}00]_\alpha$. The randomness of the atom species on the middle layer corresponds to the lack of fractional indexed ordered streaks in the experimental $[11\bar{2}0]_\alpha$ diffraction pattern, Fig. 9b. DFT calculations show that the two columns close to each other within a period can be stable instead of merging into one in the η' phase only when Ca atoms are in the middle layer, Fig. 3c. Based on the proposed atomic model of the η'' phase, four DFT supercells with different configurations are built by SQS following the elemental ratio on each mixed site. The four supercells show mechanical and thermodynamic stabilities after structural relaxations using DFT with close formation energies. In addition to the stability, the proposed mixed atomic model is further validated by the well-matched intensities of atomic columns between experimental and simulated STEM images and the matched diffraction patterns. Note that the experimentally measured Zn/Ca ratio of the *η''* varies within a small range, Fig. 4b. It is likely that the *η''* phase could adopt a different Zn/Ca ratio because many similar structures of different compositions with low formation energies per solute are also found in our DFT calculations.

Fig. 10 shows the proposed atomic structure of the *η'* phase embedded in the Mg matrix along the $[1\bar{1}00]_\alpha$ and $[11\bar{2}0]_\alpha$ directions. This phase is proposed to be $Mg_4Ca_2Zn_3$ ($P\bar{6}2$ m, $a = 0.55$ nm and $c = 0.49$ nm) with the Zn/Ca ratio of 3:2. Compared to the *η''* phase, the two side layers of the tri-layer *η'* also have an ordered pattern with Ca atoms six-folded coordinated by Mg atoms on the basal plane but with no mixed atoms. Because the atomic intensities of the Mg columns in the side layers are the same as those of Mg columns in the matrix in the experimental $[1\bar{1}00]_\alpha$ STEM images, Fig. 3c, which indicates few solutes in the Mg columns. Additionally, the intensities of Ca columns are stronger than those of Mg columns in the matrix, Fig. 3c, which is different from the case in *η'', i.e.*, Ca-rich columns having equal or dimmer intensities than Mg columns in the matrix, Fig. 3b. The ordered pattern on the two side layers of the *η'* corresponds to the streaks of the 1/3 and 2/3 $[11\bar{2}0]_\alpha$ on the experimental $[1\bar{1}00]_\alpha$ diffraction pattern, Fig. 10a. The middle layer of the tri-layer *η'* only consists of pure Zn atoms, which corresponds to the lack of fractional indexed ordered streaks in the experimental $[11\bar{2}0]_\alpha$ diffraction pattern, Fig. 10b. Based on the proposed atomic structure in Fig. 10, the DFT supercell is built, and the cell shows mechanical and thermodynamic stabilities after structural relaxations using DFT. Furthermore, the simulated STEM images and diffraction patterns of the proposed *η'* phase agree with the experimental ones, which further confirms the validity of the proposed structure. Compared with the *η''* phase, the *η'* phase shows a more ordered structure with an increased concentration of Zn, which means the partially ordered *η''* phase can be a structural precursor for the ordered *η'* phase. Notice that the tri-layer structures are similar to $CaCu_5$-type Laves phases. It is likely that the attractive chemical interaction and the repulsive strain interaction due to the large and anisotropic lattice mismatch together lead to such local arrangements. Similar transition path from configurations on the HCP lattice to Laves phases have been reported in binary Mg-Zn systems [51,52].

After prolonged aging to 100 h, the *η'* plates tend to form in pairs followed by stacks, Figs. 2e and f, with the interplanar spacing mostly concentrated in 5 α-Mg layers, Figs. 5a through d. We explained the thermodynamic origin behind that transformation by DFT calculations encoding both strain and interfacial free energies. Based on the atomic structure of *η'* phase ($Mg_4Ca_2Zn_3$), we build a supercell with two tri-layer *η'* plates separated by 1 to 7 Mg layers within the Mg matrix of 30 atomic layers along the $[0001]_\alpha$, Fig. 11a. The Mg layers in the matrix are used to separate the interaction between *η'* plates due to periodic boundaries in DFT calculations. As shown in Fig. 11b, the formation energy of the whole supercell decreases rapidly when the number of the separating Mg layers varies from 1 to 4, and gradually increases from 4 to 7. The system reaches the minimum energy when the number of the Mg layers is around 4, which is quite close to the experimental observations, Figs. 5a-d. That is similar to the case of the inter-plate distance of γ'' precipitates in Mg-6Y-2Ag-1Zn-0.6Zr (wt.%) alloy [18]. Therefore, the presence of 4–5 atomic layers of Mg is the most energetically stable when forming a plate pair of *η'* plates, likely due to the competition between attractive chemical and repulsive strain interactions between plates of *η'*.

Coarse η_1 plates heterogeneously formed in the matrix during overaging, as shown in Figs. 5e through h and Fig. S.4. A similar long-period superlattice structure was reported for the $Mg_{17}Zn_3Yb_4$; $P\bar{6}2m$, $a = 0.6$ nm, $c = 1.02$ nm in a high-pressure synthesized $Mg_{97}Zn_1Yb_2$ alloy [53], while such η_1 thick plate, to our best knowledge, is firstly

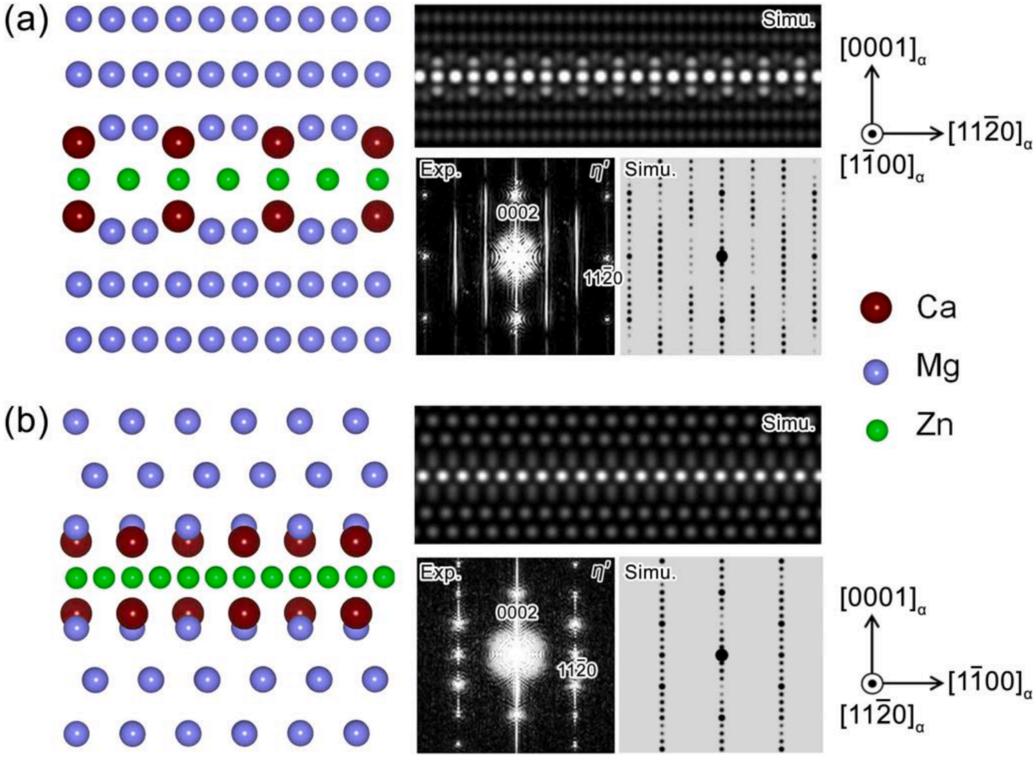

Fig. 10. The proposed atomic models, simulated STEM images, and diffraction patterns of the *η'* phase embedded in Mg matrix viewed along the (a) $[1\bar{1}00]_\alpha$ and (b) $[11\bar{2}0]_\alpha$ directions.

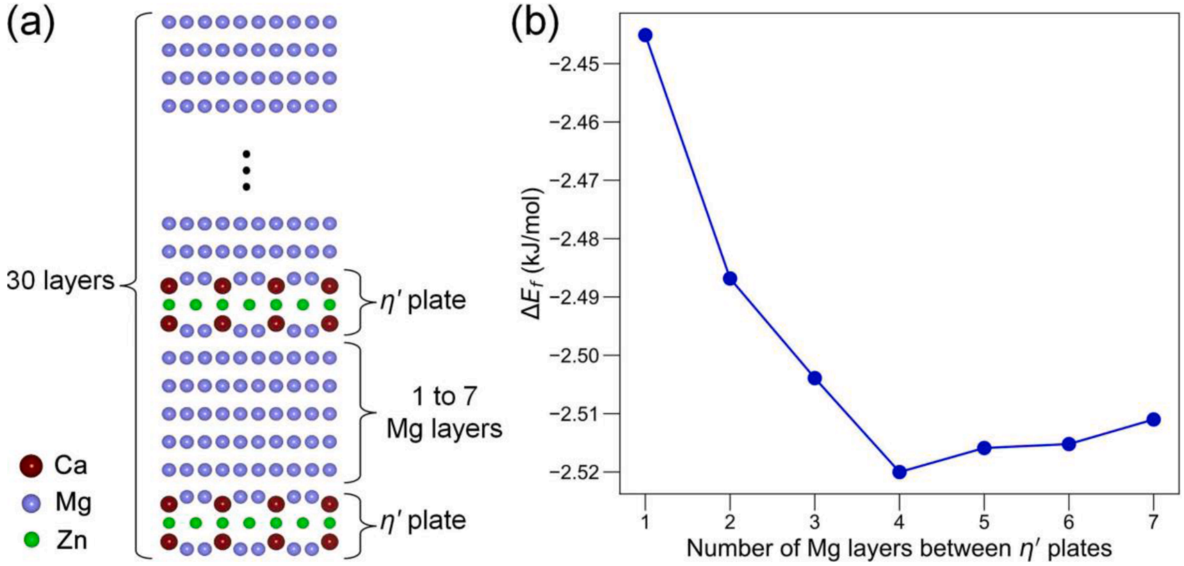

Fig. 11. (a) Schematic diagram of the supercell with various number of Mg layers between two η' plates along $[0001]_\alpha$ direction. (b) Variation of formation energy as a function of number of Mg layers.

observed in the Mg-Ca-Zn alloys. Based on the imaging contrast in the HAADF-STEM image, Figs. 5e and f, and DFT calculations, $Mg_7Ca_2Zn_3$ (Pm, $a = 0.57$ nm, $b = 2.26$ nm, $c = 0.97$ nm, $\beta = 120°$) is proposed as the η_1 phase. The unit structure, as shown in Fig. 12a, contains 4 layers along the $[0001]_{\eta1}$, including a tri-layer substructure like η''/η' and an additional layer of atoms concentrated with Zn and Mg atoms separating

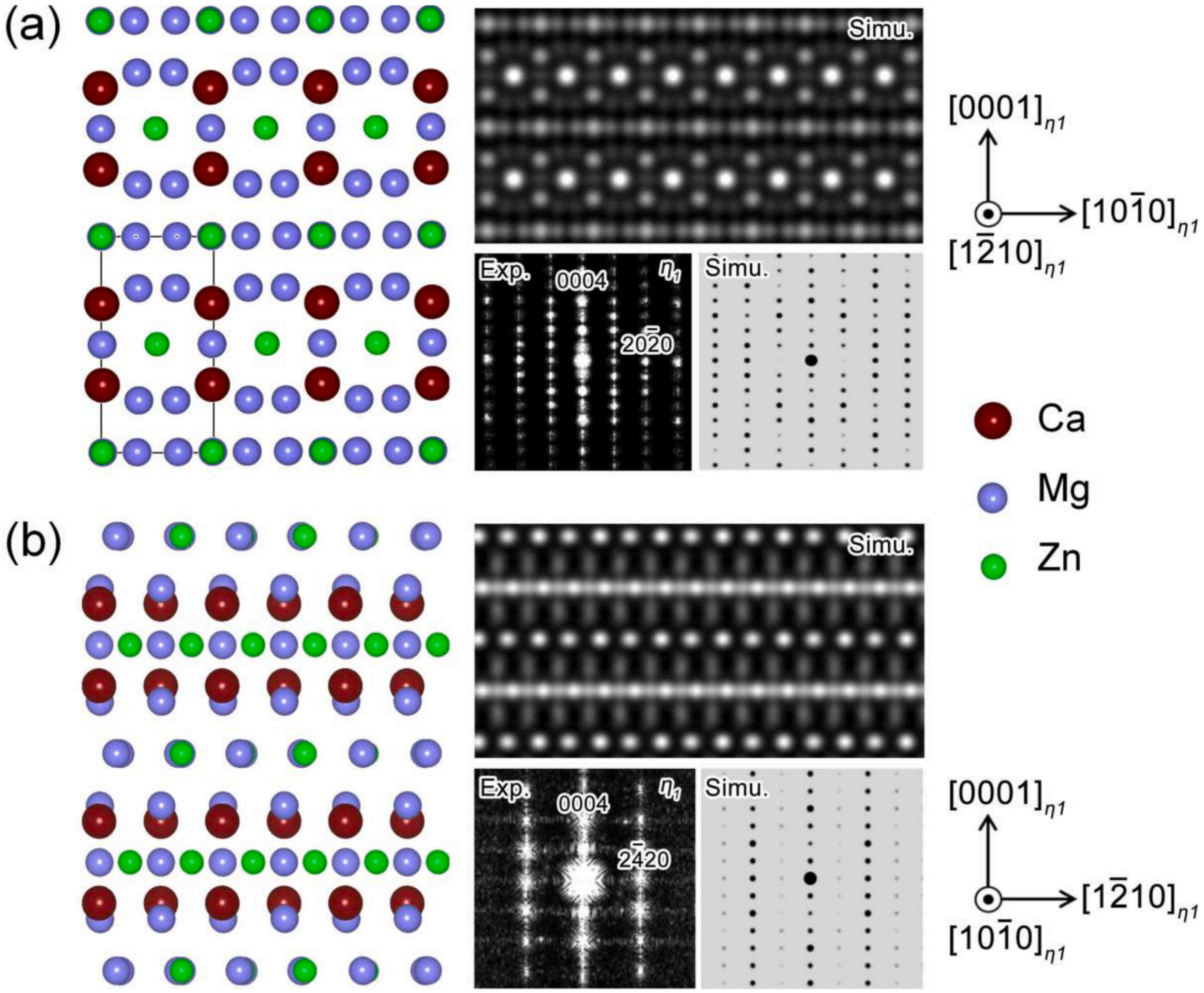

Fig. 12. The proposed atomic models, simulated STEM images, and diffraction patterns of the η_1 phase viewed along the (a) $[1\bar{2}10]_{\eta1}$ and (b) $[10\bar{1}0]_{\eta1}$ directions.

the tri-layer substructures. The separating layer has the same periodicity of three atomic columns on this plane, which agrees with the tri-layer substructure as shown in the experimental HAADF-STEM image along the $[1\bar{1}00]\alpha$ direction, Fig. 5f. Based on the intensities of atomic columns on the separating layer, the brightest spot within a periodicity correspond to the Zn-rich column with a Zn/Mg ratio of 1/1, and the two weak spots corresponds to two Mg-rich columns with a Zn/Mg ratio of 1/3. Within the tri-layer substructure, the two side layers are the same as that of η''/η', and the inner layer has a composition of $MgZn_2$, which leads to the overall composition of $Mg_7Ca_2Zn_3$ for the η_1 phase. Besides, the simulated patterns STEM and SAED patterns are also well consistent with the experimental ones, Figs. 12a and b. These results confirm the proposed structure for the η_1 phase.

The equilibrium η phase has a hexagonal structure of $Mg_{10}Ca_3Zn_6$; $P6_3/mmc$ with $a = 1.00$ nm and $c = 1.01$ nm, Fig. 7, similar to the recently reported $Ca_2Mg_5Zn_5$ [25]. However, the concentration of Zn; ~ 30 at.% is lower than that in $Ca_2Mg_5Zn_5$; ~ 42 at.%. Within the unit cell of the proposed atomic model of η phase by HAADF-STEM analysis, 11 atomic columns are occupied by either Zn or Mg along the $[0001]_\eta$ direction with the Zn/Mg ratio of 3:1 or 1:1 on each atomic site, as shown by the mixed atomic symbols in Fig. 13a. The atomic model viewed from $[11\bar{2}0]_\eta$ and $[1\bar{1}00]_\eta$ are shown in Figs. 13b and c, respectively. Based on this atomic model, the STEM images and SAED patterns are simulated along the $[0001]_\eta$, $[11\bar{2}0]_\eta$, and $[1\bar{1}00]_\eta$, and these simulated results are consistent with the experimental patterns in Fig. 7.

Structures with definitive configurations must be chosen for those mixed sites in DFT calculations to analyze the thermodynamic stability of the atomic model of the η phase in Fig. 13. Considering the disordering on those mixed sites and the ordering pattern based on the experimentally determined group symmetry (*i.e.*, $P6_3/mmc$), both disordered and ordered supercells of the η phase were built. For the disordered ones, 6 different structures with Mg and Zn atoms randomly occupying the mixed sites were built using SQS following the elemental fraction of the proposed atomic model. For ordered configurations, the structures with definitive atomic occupations on mixed sites were enumerated to find the ones with the space group of $P6_3/mmc$. The search process is: (i) 3612 possible structures in the proposed atomic model of 38 atoms were enumerated on the non-determined mixed sites; (ii) 10 structures were selected after limiting the concentration of Mg to 49–61 at.%, and the point group form the NBED pattern (listed in Tables S.1 and S.2); (iii) 2 structures with the composition of $Mg_{10}Ca_3Zn_6$ showing the space group of $P6_3/mmc$ ($a = 0.96$ nm, $c = 1.03$ nm) after structural optimization in DFT were determined as the final candidates. Fig. S.6 shows the simulated HAADF-STEM and SAED patterns of two ordered η candidates. Their SAED patterns agree well with the experimental results, while the HAADF-STEM images have a minute difference compared with the experiments. This difference confirms the disordering on the mixed sites since the simulated and the experimental STEM images only match when considering the statistically averaged effect of atomic columns on the mixed sites (Fig. 13). Further, the structures with 6 random configurations and 2 ordered configurations on the mixed sites of η phase have the same composition and very close formation energies in DFT calculations, *i.e.*, from −15.437 to −14.887 kJ/mol, which explains the disordering of Mg and Zn on those mixed sites of η phase.

To explore the thermodynamic stabilities of these phases, we calculated their formation energy per solute, *i.e.*, E_f^{solute}, based on the proposed atomic structures. In addition to these phases, the formation energy of ordered monolayer G.P. zones and solid solutions are also included for a complete picture [15]. The E_f^{solute} is analyzed as a function of $x_{Zn}/(x_{Zn}+x_{Ca})$ to facilitate a comparison of structures with varying Mg concentration but fixed Zn/Ca ratios [39,40]. As shown in Fig. 14, the E_f^{solute} decrease is generally consistent with the observed precipitation sequence: S.S.S.S → G.P. zones → η'' → η' / η_1 → η. Additionally, the Zn/Ca ratio generally increases along this sequence, which shows a correlation between decreasing energy and increasing Zn/Ca ratio as precipitation process proceeds. Note that the proposed η_1 phase has a slightly higher E_f^{solute} than that of η', which indicates the proposed η_1

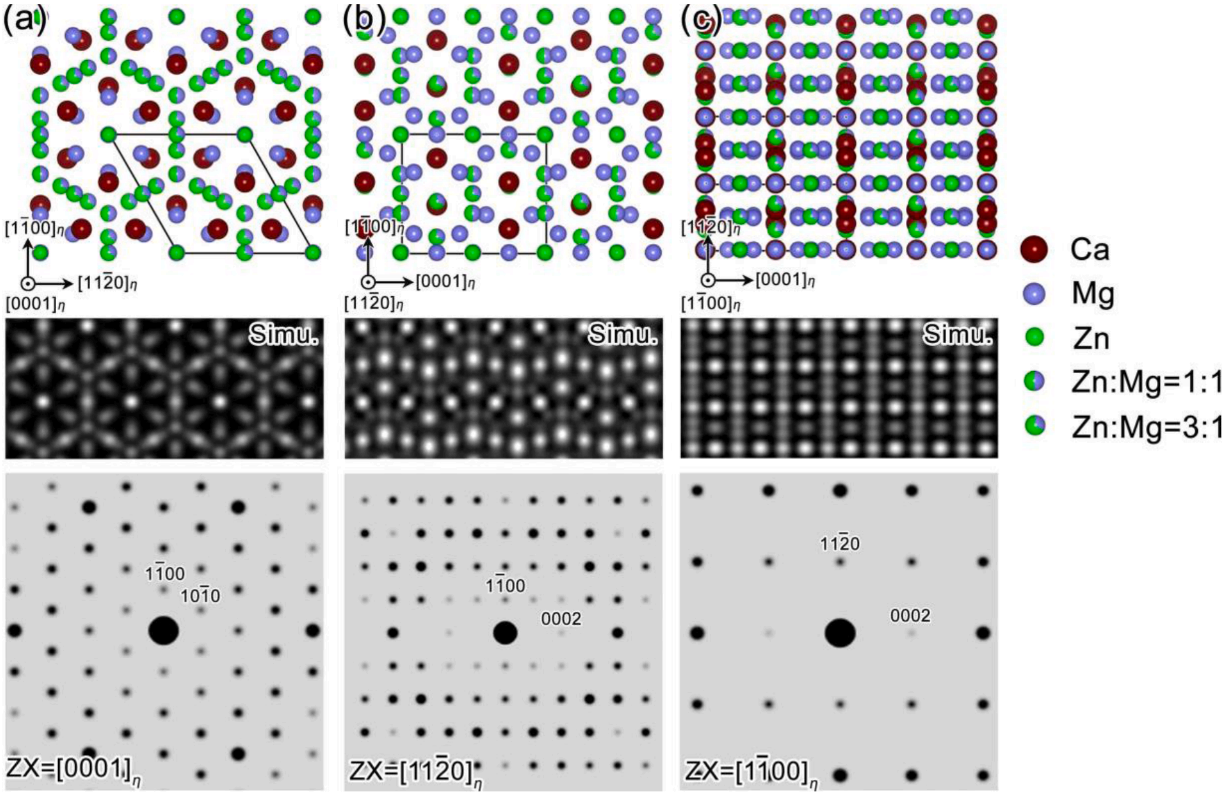

Fig. 13. The proposed atomic models, simulated STEM images, and SAED patterns of the η phase viewed along the (a) $[0001]_\eta$, (b) $[11\bar{2}0]_\eta$, and (c) $[1\bar{1}00]_\eta$ directions.

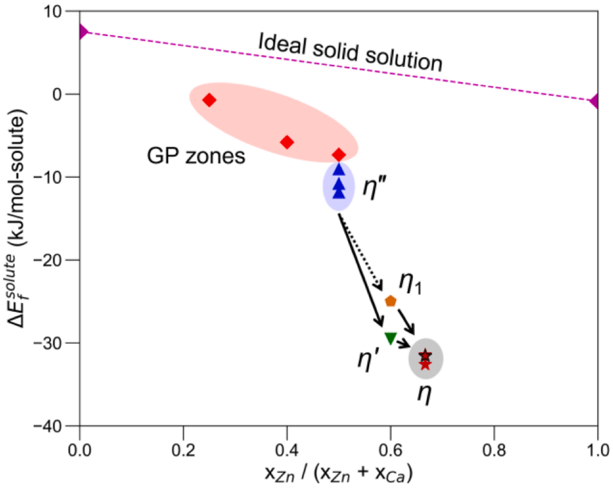

Fig. 14. Formation energy per solute E_f^{sloute} of series of precipitates observed during the aging process.

phase can be less stable than η'. As discussed before, the formation of the η_1 phase is likely to be facilitated by defects, while the effect of defects on its formation energy is not incorporated in first-principles calculations due to the small simulation cells. Despite the small difference, the energies per solutes for η_1 and η' are close, indicating that they are likely to coexist in experiments. In addition, atomic-resolution STEM observations also show the structural transformations from η' plates and pairs to the η_1 via the thickening process and in-situ solute rearrangements, respectively, Fig. S.5. Considering that the η' and η_1 phases have the similar thermal stabilities, the η_1 phase may shows a larger size and number density than the η' as the aging temperature increases, due to the fact that the higher temperature can facilitate the solute diffusion to the η_1 containing more solutes. For the η phase, the formation energies per solute of structures with random occupations are marked by black stars, while the ordered ones with a space group of P6$_3$/mmc are marked by red stars. The energies marked by both black and red stars are very close, indicating that these structures of η are nearly equally probable to be observed experimentally and their coexistence leads to the mixed sites in the observed η phase.

These observations have shown that ZX20 alloy experiences a similar transformation path, from SSSS to η_1, to the Mg-RE-Zn system, from SSSS to γ' [17]. Nevertheless, the aspect ratio of the η_1 plates (∼ 150:1) is much smaller than that of the γ' plates (over 1000:1) [17,18]. The difference in stacking sequence between the η_1 and γ' may explain such different morphologies. The γ' has an ···ABCABC··· stacking ordered structure on the $(0002)_\alpha$ plane compared to the γ'', ··ABAB··. The large shear strain (∼0.35) during the hcp/fcc transformation from the γ'' to γ' leads to the large aspect ratio of the γ' in order to minimize the strain energy of the entire system. In contrast, the η_1 maintains the similar ··ABAB·· stacking sequence to that of the η' and shows a relatively small lattice misfit of only −0.07 along the $[0001]_\alpha$direction and near zero within the $(0002)_\alpha$ habit plane, Figs. 5e and f. Thus, the relatively low volumetric strain energy leads to the thickening of the η_1 plate rather than broadening the surface within the $(0002)_\alpha$ plane. In addition, the solute-enriched stacking fault structure is reported to be thermodynamically unstable in the Mg-Ca-Zn system [54]. This may also explain the different precipitation behaviors between the Mg-Ca-Zn and Mg-RE-Zn alloys.

The age-hardening response of the ZX20 alloy is closely related to the microstructure of precipitates during isothermal aging. Table 2 summaries the size, number density, and volume fraction of precipitates at various aging times. Note that the volume fraction was estimated from the product of the mean volume and the number density. The ZX20 alloy shows the maximum hardness increment, ΔHv of 13.5 HV by peak-aging at 0.3 h, which is mainly attributed to a large number of monolayer G.P. zones; ∼ 1.2×10^{24} m^{-3} formation in the matrix. According to the APT results, the Zn and Ca concentrations within the matrix decrease from 0.35 to 0.13 at.% to 0.23 and 0.07 at.%, respectively, during the 0.3 to 10 h-aging. The change in solid solution strengthening for basal slip is estimated to be ∼ 2.2 MPa (∼ 0.23 HV) based on the obstacle model from Yasi et al. [55], which suggests a slight strengthening effect in the early stages of aging. Assuming that the G.P. zones, η'', and η' are shearable precipitates, the stress increment for basal slip is given as [56]:

Table 2
Size, number density and volume fraction of precipitates at various aging times.

Aging time, h	Precipitate	Size Diameter, nm	 Thickness, nm		Number density, m^{-3}	Volume fraction,%
0.3	G.P. zone	3.6 ± 0.8	0.17		1.2×10^{24}	0.2
2	η''	7.8 ± 1.3	0.47		4.5×10^{23}	1
10	η'	14.7 ± 3.2	0.46		1.6×10^{23}	1.3
100	η' *pair*	45.3 ± 8.7	0.46		3.7×10^{22}	2.8
		Length, nm	Width, nm	Thickness, nm		
1000	η	350 ±100	80 ±40	30 ±10	8.1×10^{19}	3.4

$$\Delta\sigma = \left(\frac{\alpha d_p}{2b}\right)^{3/2}\left(\frac{\mu b}{\frac{1}{\sqrt{N_v t}} - d_p}\right) \tag{1}$$

where α is the obstacle strength, d_p is mean precipitate diameter on the slip plane, b is the Burgers vector of the basal dislocations; ∼ 0.32 nm, μ is the shear modulus of α-Mg; ∼ 17.2 GPa, N_v and t are the number density and the thickness of basal plates. The obstacle strength of the G.P. zone using Eq. (1) is calculated to be 0.166, which is similar to the previous report [57]. The following 2 h aging shows the retention of hardness increment; ΔHv = ∼ 13.3 HV due to the slightly decreased number density; ∼ 4.5×10^{23} m^{-3} while increased size of η''. The α_{basal} of the η'' is calculated to be ∼ 0.105, which is lower than that of the G.P. zone. The hardness gradually degrades in the subsequent over-aging because the decrease in number density outweighs the increase in precipitate size. The 10 h-aged sample show the ΔHv of ∼ 9.6 HV, resulting in a lower α_{basal} of 0.063 for the η' compared to the η''. Therefore, the G.P. zones are the strongest precipitate in the Mg-Ca-Zn system. After extended 100 h-aging, the hardness value of the ZX20 alloy is even lower than that in the as-quenched condition; ΔHv = ∼ −1.8 HV, indicating that the strengthening by precipitates is totally offset by the reduction of solutes in the matrix during precipitation. The volume fraction of the η phase in the 1000 h-aged sample is measured to be ∼ 3.4%, which is slightly higher than the calculated value, ∼ 1% in the reported phase diagram [25].

Summary

In this work, we thoroughly investigated the precipitation process and the structures of precipitates in the ZX20 alloy with a combined use of HAADF-STEM imaging, 3DAP, and DFT calculations. The main conclusions are summarized as follows:

1 Precipitation during isothermal aging at 200 °C involves the evolution from the G.P. zones to the equilibrium η phase, and the formation of a series of metastable phases; η'', η', and η_1 in the intermediate process. A precipitation sequence is proposed as:

S.S.S.S. → G.P. zones → η'' → η' → η' pairs and stacks / η_1 → η

The formation energies per solute of each phase decrease along this precipitation sequence in DFT calculations, which provides thermodynamic reasoning behind the observed sequence.

2. The monolayer G.P. zones in the peak-aged sample transform to the η'' and η' $(0001)_\alpha$ plates with single unit-cell height during the over-aging. The Zn/Ca ratio of plates evolves from 1 to 1.5. The η'' has a disordered hexagonal structure; Pm, $a = 0.55$ nm, $c = 0.53$ nm and a composition of $Mg_5Ca_2Zn_2$, while η' has a composition of $Mg_4Ca_2Zn_3$ with a symmetry group of $P\bar{6}2\,m$, $a = 0.55$ nm, $c = 0.49$ nm. The crystal structures and atomic occupancies of η'' and η' were deduced through a synthesis of the information from STEM, 3DAP, and DFT calculations.
3. The η' plates develop into pairs and stacks with the interplanar spacing most in ~ 4 to 5 α-Mg layers after 100 h aging. This spacing is proven to be the most energetically stable in DFT for the stacking of η' plates in the Mg matrix. Coarse η_1 plates (Pm, $a = 0.57$ nm, $c = 0.97$ nm) also heterogeneously form on the $(0002)_\alpha$ plane with a composition of $Mg_7Ca_2Zn_3$. The orientation relationship between the η_1 and the α-Mg matrix is such that $(0001)_{\eta_1} // (0001)_\alpha$, $[1\bar{1}00]_{\eta_1} // [11\bar{2}0]_\alpha$.
4. The equilibrium η phase has a hexagonal structure; $P6_322$, $a = 0.96$ nm, $c = 1.03$ nm with a composition of $Mg_{10}Ca_3Zn_6$. The orientation relationship between the rhombic-shaped η basal plate and the α-Mg matrix is described as $(11\bar{2}0)_\eta // (0001)_\alpha$, $[0001]_\eta // [11\bar{2}0]_\alpha$, while the lath-shaped η non-basal plate is such that $(01\bar{1}0)_\eta // (1\bar{1}03)_\alpha$, $[0001]_\eta // [11\bar{2}0]_\alpha$. The mixed Mg/Zn sites within the phase are confirmed by DFT calculations, which leads to the statically averaged effect on the atomic column intensities in the experimental HAADF-STEM results.

Declaration of Competing Interest

The authors declare that they have no known competing financial interests or personal relationships that could have appeared to influence the work reported in this paper.

Acknowledgments

ZL, TS, TO, KH would like to acknowledge financial support from JSPS KAKENHI [Grant Number JP21H01675], the Light Metal Educational Foundation, Inc., and Element Strategy Initiative of MEXT [Grant Number JPMXP0112101000]. DC, KW, ERH, JMH, and BCZ would like to acknowledge financial support from the U.S. National Science Foundation (NSF) DMREF grant CMMI-1921926 that is supervised by Dr. Alexis C. Lewis. DC, KW, and BCZ acknowledge Research Computing at The University of Virginia (https://rc.virginia.edu) for providing computational resources and technical support that have contributed to the results reported within this publication. This work also used the Extreme Science and Engineering Discovery Environment (XSEDE) resources, which is supported by NSF grant number ACI-1548562, via the Stampede2 supercomputer at the Texas Advanced Computing Center. The authors thank Dr. Helge Heinrich for his great contribution to the calculation of Pendellösung plots.

Supplementary materials

Supplementary material associated with this article can be found, in the online version, at doi:10.1016/j.actamat.2023.119072.

References

[1] S. You, Y. Huang, K.U. Kainer, N. Hort, Recent research and developments on wrought magnesium alloys, J. Mag. Alloys 5 (2017) 239–253.

[2] Y. Chen, Z. Xu, C. Smith, J. Sankar, Recent advances on the development of magnesium alloys for biodegradable implants, Acta Biomater 10 (2014) 4561–4573.

[3] C.L. Mendis, K. Oh-ishi, Y. Kawamura, T. Honma, S. Kamado, K. Hono, Precipitation hardenable Mg–2.4Zn–0.1Ag–0.1Ca–0.16Zr (at.%) wrought magnesium alloy, Acta Mater 57 (2009) 749–760.

[4] Z.H. Li, T.T. Sasaki, T. Shiroyama, A. Miura, K. Uchida, K. Hono, Simultaneous achievement of high thermal conductivity, high strength and formability in Mg-Zn-Ca-Zr sheet alloy, Mater. Res. Lett. 8 (2020) 335–340.

[5] M.Z. Bian, T.T. Sasaki, T. Nakata, Y. Yoshida, N. Kawabe, S. Kamado, K. Hono, Bake-hardenable Mg-Al-Zn-Mn-Ca sheet alloy processed by twin-roll casting, Acta Mater 158 (2018) 278–288.

[6] Z.H. Li, T.T. Sasaki, T. Shiroyama, A. Miura, K. Uchida, K. Hono, Role of Zn on the rapid age-hardening in Mg-Ca-Zn alloys, Scr. Mater. 216 (2022), 114735.

[7] X. Gao, S.M. Zhu, B.C. Muddle, J.F. Nie, Precipitation-hardened Mg–Ca–Zn alloys with superior creep resistance, Scr. Mater. 53 (2005) 1321–1326.

[8] M. Cihova, E. Martinelli, P. Schmutz, A. Myrissa, R. Schäublin, A.M. Weinberg, P. J. Uggowitzer, J.F. Löffler, The role of zinc in the biocorrosion behavior of resorbable Mg−Zn−Ca alloys, Acta. Biomater. 100 (2019) 398–414.

[9] P. Holweg, L. Berger, M. Cihova, N. Donohue, B. Clement, U. Schwarze, N. G. Sommer, G. Hohenberger, J. van den Beucken, F. Seibert, A. Leithner, J. F. Loffler, A.M. Weinberg, A lean magnesium-zinc-calcium alloy ZX00 used for bone fracture stabilization in a large growing-animal model, Acta Biomater. 113 (2020) 646–659.

[10] J.F. Nie, Precipitation and hardening in magnesium alloys, Metall. Mater. Trans. A 43A (2012) 3891–3939.

[11] D.H. Ping, K. Hono, J.F. Nie, Atom probe characterization of plate-like precipitates in a Mg–RE–Zn–Zr casting alloy, Scr. Mater. 48 (2003) 1017–1022.

[12] J.C. Oh, T. Ohkubo, T. Mukai, K. Hono, TEM and 3DAP characterization of an age-hardened Mg–Ca–Zn alloy, Scr. Mater. 53 (2005) 675–679.

[13] K. Oh-ishi, R. Watanabe, C.L. Mendis, K. Hono, Age-hardening response of Mg–0.3 at.% Ca alloys with different Zn contents, Mater. Sci. Eng. A 526 (2009) 177–184.

[14] B. Langelier, X. Wang, S. Esmaeili, Evolution of precipitation during non-isothermal ageing of an Mg-Ca-Zn alloy with high Ca content, Mat. Sci. Eng. A 538 (2012) 246–251.

[15] D. Cheng, E.R. Hoglund, K. Wang, J.M. Howe, S.R. Agnew, B. Zhou, Atomic structures of ordered monolayer GP zones in Mg-Zn-X (X= Ca, Nd) systems, Scr. Mater. 216 (2022), 114744.

[16] J.F. Nie, B.C. Muddle, Precipitation hardening of Mg-Ca (-Zn) alloys, Scr. Mater. 37 (1997) 1475–1481.

[17] J.F. Nie, K. Oh-ishi, X. Gao, K. Hono, Solute segregation and precipitation in a creep-resistant Mg–Gd–Zn alloy, Acta Mater 56 (2008) 6061–6076.

[18] Y.M. Zhu, K. Oh-ishi, N.C. Wilson, K. Hono, A.J. Morton, J.-F. Nie, Precipitation in a Ag-containing Mg-Y-Zn Alloy, Metall. Mater. Trans. A 47 (2016) 927–940.

[19] K. Saito, M. Nishijima, K. Hiraga, Stabilization of Guinier-Preston zones in hexagonal close-packed Mg-Gd-Zn alloys studied by transmission electron microscopy, Mate. Trans. 51 (2010) 1712–1714.

[20] K. Saito, A. Yasuhara, K. Hiraga, Microstructural changes of Guinier-Preston zones in an Mg–1.5at.%Gd–1at.%Zn alloy studied by HAADF-STEM technique, J. Alloy Compd. 509 (2011) 2031–2038.

[21] G. Levi, S. Avraham, A. Zilberov, M. Bamberger, Solidification, solution treatment and age hardening of a Mg–1.6wt.% Ca–3.2wt.% Zn alloy, Acta Mater 54 (2006) 523–530.

[22] P.M. Jardim, G. Solorzano, J.B. Vander Sande, Precipitate crystal structure determination in melt spun Mg-1.5wt%Ca-6wt%Zn alloy, Microsc. Microanal. 8 (2002) 487–496.

[23] Y.-N. Zhang, D. Kevorkov, F. Bridier, M. Medraj, Experimental study of the Ca-Mg-Zn system using diffusion couples and key alloys, Sci. Technol. Adv. Mat. 12 (2011), 025003.

[24] J.D. Cao, T. Weber, R. Schäublin, J.F. Löffler, Equilibrium ternary intermetallic phase in the Mg-Zn-Ca system, J. Mater. Res. 31 (2016) 2147–2155.

[25] R.E. Schäublin, M. Becker, M. Cihova, S.S.A. Gerstl, D. Deiana, C. Hébert, S. Pogatscher, P.J. Uggowitzer, J.F. Löffler, Precipitation in lean Mg–Zn–Ca alloys, Acta Mater 239 (2022), 118223.

[26] S.M. Allen, Foil thickness measurements from convergent-beam diffraction patterns, Ultramicroscopy 90 (2002) 71–83.

[27] K. Ishizuka, A practical approach for STEM image simulation based on the FFT multislice method, Philos. Mag. A 43 (1981) 325–335.

[28] D. Vaumousse, D. Cerezo, P.J. Warren, A procedure for quantification of precipitate microstructures from three-dimensional atom probe data, Ultramicroscopy 95 (2003) 215–221.

[29] E.A. Jägle, P.P. Choi, D. Raabe, The maximum separation cluster analysis algorithm for atom-probe tomography: parameter determination and accuracy, Microsc. Microanal. 20 (2014) 1662–1671.

[30] A. Zunger, S.H. Wei, L.G. Ferreira, J.E. Bernard, Special quasirandom structures, Phys. Rev. Lett. 65 (1990) 353.

[31] A. van de Walle, P. Tiwary, M. de Jong, D.L. Olmsted, M. Asta, A. Dick, D. Shin, Y. Wang, L.Q. Chen, Z.K. Liu, Efficient stochastic generation of special quasirandom structures, Calphad 42 (2013) 13–18.

[32] A. van de Walle, Multicomponent multisublattice alloys, nonconfigurational entropy and other additions to the alloy theoretic automated toolkit, Calphad 33 (2009) 266–278.

[33] W. Kohn, L.J. Sham, Self-consistent equations including exchange and correlation effects, Phys. Rev. 140 (1965) A1133.

[34] P. Hohenberg, W. Kohn, Inhomogeneous electron gas, Phys. Rev. 136 (1964) 864.

[35] D. Joubert, From ultrasoft pseudopotentials to the projector augmented-wave method, Phys. Rev. B 59 (1999) 1758–1775.

[36] J.P. Perdew, K. Burke, M. Ernzerhof, Generalized gradient approximation made simple, Phys. Rev. lett. 77 (1996) 3865–3868.

[37] G. Kresse, Efficient iterative schemes for ab-initio total-energy calculations using a plane-wave basis set, Phys. Rev. B. 54 (1996) 11169–11186.

[38] G. Kresse, J. Furthmuller, Efficiency of ab-initio total energy calculations for metals and semiconductors using a plane-wave basis set, Comput. Mater. Sci. 6 (1996) 15–50.

[39] C. Ravi, C. Wolverton, First-principles study of crystal structure and stability of Al-Mg-Si-(Cu) precipitates, Acta Mater. 52 (2004) 4213–4227.

[40] D. Wang, M. Amsler, V.I. Hegde, J.E. Saal, A. Issa, B.C. Zhou, X. Zeng, C. Wolverton, Crystal structure, energetics, and phase stability of strengthening precipitates in Mg alloys: a first-principles study, Acta Mater. 158 (2018) 65–78.

[41] Z. Li, J. Zheng, B. Chen, Unravelling the structure of γ'' in Mg-Gd-Zn: an atomic-scale HAADF-STEM investigation, Mater. Charact. 120 (2016) 345–348.

[42] X. Gu, T. Furuhara, T. Kiguchi, T.J. Konno, L. Chen, P. Yang, On the atomic structure of γ'' phase in Mg-Zn-Gd alloy, Scr. Mater. 146 (2018) 64–67.

[43] H. Xie, H. Pan, Y. Ren, S. Sun, L. Wang, H. Zhao, B. Liu, X. Qi, G. Qin, Magnesium alloys strengthened by nanosaucer precipitates with confined new topologically close-packed structure, Cryst. Growth Des. 18 (2018) 5866–5873.

[44] R.K.W. Marceau, G. Sha, R. Ferragut, A. Dupasquier, S.P. Ringer, Solute clustering in Al–Cu–Mg alloys during the early stages of elevated temperature ageing, Acta Mater. 58 (2010) 4923–4939.

[45] M.W. Zandbergen, Q. Xu, A. Cerezo, G.D.W. Smith, Study of precipitation in Al–Mg–Si alloys by atom probe tomography I. Microstructural changes as a function of ageing temperature, Acta Mater. 101 (2015) 136–148.

[46] K. Buchanan, K. Colas, J. Ribis, A. Lopez, J. Garnier, Analysis of the metastable precipitates in peak-hardness aged Al-Mg-Si(-Cu) alloys with differing Si contents, Acta Mater. 132 (2017) 209–221.

[47] B. Gault, M.P. Moody, J.M. Cairney, S.P. Ringer, Atom Probe Microscopy, Springer, New York, 2012.

[48] J.P. Morniroli, J.W. Steeds, Microdiffraction as a tool for crystal structure identification and determination, Ultramicroscopy 45 (1992) 219–239.

[49] B.F. Buxton, J.A. Eades, J.W. Steeds, G.M. Rackham, The symmetry of electron diffraction zone axis patterns, Philos. Trans. Royal Soc. A 281 (1976) 171–194.

[50] T. Hahn, International Table for Crystallography, Volume A: Space-Group Symmetry, 5th ed., Springer, New York, 2005.

[51] D. Cheng, K. Wang, B.C. Zhou, Crystal structure and stability of phases in Mg-Zn alloys: a comprehensive first-principles study, Acta Mater. 242 (2023), 118443.

[52] A.R. Natarajan, A. Van der Ven, Connecting the simpler structures to topologically close-packed phases, Phys. Rev. Lett. 121 (2018), 255701.

[53] N. Fujita, M. Matsushita, R. Tsukamoto, M. Yamasaki, Y. Kawamura, T. Irifune, E. Abe, The structure of a novel long-period superlattice phase in $Mg_{97}Zn_1Yb_2$ alloys, Scr. Mater. 150 (2018) 78–81.

[54] M. Egami, I. Ohnuma, M. Enoki, H. Ohtani, E. Abe, Formation and stability of solute enriched stacking fault in the Mg–Zn–Y, Mg–Co–Y and Mg–Zn–Ca ternary systems, Mater. Trans. 61 (2020) 839–848.

[55] J.A. Yasi, L.G. Hector, D.R. Trinkle, First-principles data for solid-solution strengthening of magnesium: from geometry and chemistry to properties, Acta Mater. 58 (2010) 5704–5713.

[56] J.J. Bhattacharyya, T.T. Sasaki, T. Nakata, K. Hono, S. Kamado, S.R. Agnew, Determining the strength of GP zones in Mg alloy AXM10304, both parallel and perpendicular to the zone, Acta Mater. 171 (2019) 231–239.

[57] M. Cihova, R.E. Schäublin, L.B. Hauser, S.S.A. Gerstl, C. Simson, P.J. Uggowitzer, J. F. Löffler, Rational design of a lean magnesium-based alloy with high age-hardening response, Acta Mater 158 (2018) 214–229.